UC Riverside
UC Riverside Previously Published Works

Title

Large Interferometer For Exoplanets (LIFE). XII. The Detectability of Capstone Biosignatures in the Mid-infrared—Sniffing Exoplanetary Laughing Gas and Methylated Halogens

Permalink

Journal

ISSN

Authors

Angerhausen, Daniel
Pidhorodetska, Daria
Leung, Michaela
et al.

Publication Date

DOI

Copyright Information

CrossMark

Large Interferometer For Exoplanets (LIFE). XII. The Detectability of Capstone Biosignatures in the Mid-infrared—Sniffing Exoplanetary Laughing Gas and Methylated Halogens

Daniel Angerhausen[1,2] , Daria Pidhorodetska[3] , Michaela Leung[3] , Janina Hansen[1,2] , Eleonora Alei[1,2,4] ,
Felix Dannert[1,2] , Jens Kammerer[5,6] , Sascha P. Quanz[1,2,7] , and Edward W. Schwieterman[3,8]
The LIFE initiative

[1] ETH Zurich, Institute for Particle Physics & Astrophysics, Wolfgang-Pauli-Str. 27, 8093 Zurich, Switzerland
[2] National Center of Competence in Research PlanetS, Gesellschaftsstrasse 6, 3012 Bern, Switzerland
[3] Department of Earth and Planetary Sciences, University of California, Riverside, CA, USA
[4] NPP Fellow, NASA Goddard Space Flight Center, Greenbelt, MD 20771, USA
[5] European Southern Observatory, Karl-Schwarzschild-Straße 2, 85748 Garching, Germany
[6] Space Telescope Science Institute, 3700 San Martin Drive, Baltimore, MD 21218, USA
[7] ETH Zurich, Department of Earth Sciences, Sonneggstrasse 5, 8092 Zurich, Switzerland
[8] Blue Marble Space Institute of Science, Seattle, WA 98154, USA
Received 2023 November 26; revised 2023 December 21; accepted 2023 December 29; published 2024 February 26

Abstract

This study aims to identify exemplary science cases for observing N_2O, CH_3Cl, and CH_3Br in exoplanet atmospheres at abundances consistent with biogenic production using a space-based mid-infrared nulling interferometric observatory, such as the Large Interferometer For Exoplanets (LIFE) mission concept. We use a set of scenarios derived from chemical kinetics models that simulate the atmospheric response of varied levels of biogenic production of N_2O, CH_3Cl, and CH_3Br in O_2-rich terrestrial planet atmospheres to produce forward models for our LIFESIM observation simulator software. In addition, we demonstrate the connection to retrievals for selected cases. We use the results to derive observation times needed for the detection of these scenarios and apply them to define science requirements for the mission. Our analysis shows that in order to detect relevant abundances with a mission like LIFE in its current baseline setup, we require: (i) only a few days of observation time for certain very nearby "golden target" scenarios, which also motivate future studies of "spectral-temporal" observations (ii) ~10 days in certain standard scenarios such as temperate, terrestrial planets around M star hosts at 5 pc, (iii) ~50–100 days in the most challenging but still feasible cases, such as an Earth twin at 5 pc. A few cases with very low fluxes around specific host stars are not detectable. In summary, the abundances of these capstone biosignatures are detectable at plausible biological production fluxes for most cases examined and for a significant number of potential targets.

Unified Astronomy Thesaurus concepts: Exoplanets (498); Biosignatures (2018); Infrared spectroscopy (2285); Interferometry (808)

1. Introduction

Nitrous oxide (N_2O) and methylated halogens (e.g., CH_3Cl, CH_3Br) are part of the group of molecules that have been proposed as potential biosignatures[9] for detecting life in exoplanetary contexts (see, e.g., Leung et al. 2022; Schwieterman et al. 2022). A large inferred flux of these biogenic gases is most consistent with a productive global photosynthetic biosphere, which could be revealed in tandem with O_3. None of these three gases are produced in chemical equilibrium, which reduces the false positives potential when compared to other potential biosignatures that do have equilibrium sources (e.g., CH_4, PH_3, NH_3). N_2O is produced by certain microbes during nitrification and denitrification processes, which are common in many environments on Earth. Similarly, CH_3X gases are produced by marine microbes and terrestrial plants. The short photochemical lifetimes of these gases require large production rates to sustain significant (or detectable) abundances. The detection of nitrous oxide or methylated halogens in the atmosphere of a terrestrial, temperate exoplanet could therefore indicate the presence of fluxes that can only be explained by a global biosphere of (microbial) life producing it. In the next decades, our community will start to investigate the atmospheric properties for a statistically significant, comprehensive, and consistent, large observational set of rocky, warm exoplanets (see, e.g., Fujii et al. 2018). First steps, albeit with a focus on larger planets, in this direction will be made with selected or proposed ground-based projects (see, e.g., Snellen et al. 2013; Lovis et al. 2017; Ben-Ami et al. 2018) and space-based missions such as the JWST (Greene et al. 2016; Morley et al. 2017), Roman (Kasdin et al. 2020) or the Atmospheric Remote-sensing Infrared Exoplanet Large-survey (Tinetti et al. 2018). The NASA Habitable Worlds Observatory (HWO) is a proposed flagship-class mission that aims to study planets beyond our solar system and search for signs of habitability and life by probing the exoplanets in reflected stellar light. The HWO will utilize a combination of spectroscopic and imaging techniques to explore the atmospheres and surfaces of temperate

---

[9] For a more general and detailed introduction to biosignatures, we refer to Des Marais et al. (2002), Seager et al. (2016), Krissansen-Totton et al. (2018), Schwieterman et al. (2018), and references therein.

and rocky exoplanets (National Academies of Sciences & Medicine 2021).[10]

An alternative approach to the coronagraphy-based HWO concept is to cancel out the stellar contribution and separate the thermal emission of the planet using a nulling interferometer. The Large Interferometer for Exoplanets (LIFE) is a European-lead international project with the goal of consolidating various efforts and defining a road map that leads to the launch of such a space-based mid-infrared nulling interferometer (Quanz et al. 2018, 2019, 2022). This mission will be designed with the capability to investigate the atmospheric properties of a large sample of (primarily) terrestrial exoplanets. LIFE directly addresses the scientific theme of detecting and characterizing temperate exoplanets in the MIR, which was recommended with *"highest scientific priority"* by ESA's Voyage 2050 Senior Committee report[11] as a candidate topic for a future L-class mission in the ESA Science Programme. Dannert et al. (2022), Quanz et al. (2022), and Kammerer et al. (2022) discussed the detection yield of a mission like LIFE. Konrad et al. (2022) and Alei et al. (2022b) critically checked the ability of the proposed mission to characterize an Earth twin at 10 pc and Earth analogs over its geologic history. Hansen et al. (2022) and Hansen et al. (2023) compared various technical implementations of the interferometric setup, while Matsuo et al. (2023) explored phase-space synthesis decomposition to potentially improve the sensitivity of a mission like LIFE. Konrad et al. (2023) analyzed the detectability of a Venus twin exoplanet and, in particular, how clouds impact the spectral retrieval process. The observability of exocomets with LIFE was discussed in Janson et al. (2023). Carrión-González et al. (2023) studied how LIFE can detect currently already known exoplanets and how it can leverage synergies HWO. Lastly Angerhausen et al. (2023) reported on the detectability of phosphine (PH_3) in different exoplanetary scenarios with LIFE. Here, we explore the detectability of nitrous oxide and methylated halogens with a mid-infrared space-nulling interferometer observatory like LIFE. In Section 2 we introduce the exoplanetary atmospheric chemistry models and software used to simulate the LIFE observations. Section 3 summarizes the results of our feasibility study of various observational scenarios. In Section 4 we discuss these results and their implications and conclude with our main findings.

2. Models and Simulations

2.1. Photochemical Modeling

In this study, we focus on warm, terrestrial, "Earth-like" planets. To maintain consistency, simplify reproducibility, and focus solely on examining the impact of changing surface molecular fluxes for the respective gases, we assume an Earth-like bulk atmosphere (78 % N_2, 21% O_2 by volume) along with the Earth's temperature–pressure profile, which has a globally averaged surface temperature of 288 K. We also assume a planetary radius and surface gravity identical to that of Earth ($R = 6371$ km; $g = 9.8$ m s^{-1}). We provide further details in the subsections below and the original sources for these atmospheric simulations (Leung et al. 2022; Schwieterman et al. 2022).

2.1.1. Nitrous Oxide Atmospheres

N_2O is produced by life as an intermediate product of biological denitrification, the transformation of NO_3^- to N_2 gas through multiple steps, which is an essential component of the biological nitrogen cycle on Earth. N_2O is also produced by other microbial metabolisms including the direct oxidation of ammonia by certain bacteria and archaea (Prosser & Nicol 2012). The modern biological production rate of N_2O is ≈0.4 teramole per year (10^{12} moles per year; Tmol yr^{-1}), which includes both marine and terrestrial sources (Tian et al. 2020) and results in a modern atmospheric N_2O concentration of ≈330 ppb (parts-per-billion). However, the biological N_2O flux may have varied greatly through geological time. For example, the H_2S-rich Proterozoic (2.5–0.541 Ga) oceans would have sharply limited the availability of copper, an essential component of the nitrous oxide reductase enzyme that facilitates the last step in the denitrification cycle from N_2O to N_2 (Buick 2007). In the case of severe limitation of this enzyme (or its failure to evolve on an inhabited exoplanet), the N_2O flux to the atmosphere would be limited instead by the denitrification flux of the biosphere, which is substantially greater than the modern N_2O flux. Photolysis and reactions with radical species transform atmospheric N_2O into N_2 and O_2 abiotically with an average lifetime of ≈120 yr on Earth (Prather et al. 2015), though this would vary for other host stars and atmospheric compositions (e.g., O_2 concentrations). There are no substantial surface sinks for N_2O once it is released into the atmosphere.

Schwieterman et al. (2022) used a biogeochemical model and a photochemical model to circumscribe the plausible envelope of N_2O concentrations on Earth-like exoplanets with microbial biospheres. We refer to that work for a more expansive discussion of the biological and abiotic sources and sinks of N_2O. For the purposes of this work, we are interested in what range of N_2O production fluxes can result in detectable N_2O signatures in the directly imaged thermal infrared spectra of terrestrial exoplanets with the understanding that detectability at lower production rates enhances the probability such a signature may be found.

For the cases presented here, we chose those results with Earth's modern O_2 concentration (21%) and N_2O fluxes corresponding to biological production levels of (i) 1 mol yr^{-1} (equivalently, 3.7×10^9 molecules cm^{-2} s^{-1}), (ii) 10 Tmol yr^{-1} (3.7×10^{10} molecules cm^{-2} s^{-1}), and (iii) 100 Tmol yr^{-1} (3.7×10^{11} molecules cm^{-2} s^{-1}). These values correspond to scenarios where (i) 5%–10% of Earth's denitrification flux is released as N_2O, (ii) 50%–100% of Earth's total denitrification flux is released as N_2O, and (iii) 50%–100% of the denitrification flux of an Earth-like planet with twice the nutrient availability of Earth's oceans is released as N_2O. These flux levels were obtained via biogeochemical modeling as described in Section 2 of Schwieterman et al. (2022). As points of comparison, the 100 Tmol yr^{-1} case corresponds to an N_2O flux about 3 times the modern CH_4 flux and is similar to the PH_3 flux required to generate a detectable PH_3 signature on a CO_2-rich planet orbiting an M dwarf star (Sousa-Silva et al. 2020, see their Table 3).

The chemical profiles for our N_2O detectability analyses were sourced from Schwieterman et al. (2022), which describes their generation in detail. Briefly, these abundance profiles were calculated with the photochemical model component of the *Atmos* code (Arney et al. 2016).[12] The photochemical

---

model is based originally on the work of Kasting et al. (1979) but has undergone numerous subsequent modifications and upgrades (Pavlov et al. 2001; Zahnle et al. 2006; Arney et al. 2017; Lincowski et al. 2018). The model template used here includes 50 species and 238 photochemical reactions, including all major species in Earth's modern atmosphere and the dominant photochemical destruction channels for N_2O. This version is appropriate for modeling atmospheres with substantial free oxygen concentrations ($pO_2 \geqslant 1\%$ present atmospheric level; PAL) and was previously used to model possible Earth-like atmospheric scenarios for Proxima Centauri b (Meadows et al. 2018a). The simulated atmosphere is divided into 200 layers of 0.5 km thickness with a maximum altitude of 100 km. The model incorporated recommended H_2O cross sections and reaction rate corrections from Ranjan et al. (2020). We assumed the modern Earth's temperature–pressure profile for all simulations, to isolate the unique impact of different N_2O fluxes (abundances). The chemical mixing ratio profiles were otherwise calculated self-consistently with respect to varied stellar spectra and N_2O flux levels. These chemical profiles were generated assuming host star spectra identical to those of the Sun (Thuillier et al. 2004), the K6V star HD 85512 (France et al. 2016; Loyd et al. 2016), the M5.5 Ve star Proxima Centauri (Shkolnik & Barman 2014; Loyd et al. 2018; Peacock et al. 2020), and the ultracool dwarf (M8V) star TRAPPIST-1 (Peacock et al. 2019). See Appendix C and Table C1 for the ground-level N_2O mixing ratios that correspond to each flux and host star combination.

We briefly note here that all photochemical simulations were done with 1D models using key assumptions (such as average solar zenith angle) most appropriate for rapidly rotating planets, and thus do not account for circulation impacts from synchronous rotation, which would be likely for habitable zone planets orbiting M dwarf stars. However, Chen et al. (2018) showed that the differences between full 3D and 1D predictions for abundant biosignature gases like N_2O and CH_4 differ by only $\sim$20 %, which is relatively small given the uncertainty from other intrinsic and extrinsic factors such as bulk atmospheric composition, biosignature gas production rate, and distance from the host star. Schwieterman et al. (2022) quantitatively examine the sensitivity of N_2O flux-abundance relationships to other 1D model assumptions (such as vertical mixing parameterizations and background N_2 pressure) in their Section 5.5, finding small or modest effects, and we direct the reader there for more details. We emphasize the universe of potential atmospheric compositions and planetary parameters for habitable worlds is much greater than assessed here.

2.1.2. Methylated Halogen Atmospheres

The chemical profiles of Earth-twin planets with various levels of biological CH_3Cl and CH_3Br production were sourced from Leung et al. (2022) who determined the abundance using the photochemical model part of the *Atmos* code (Arney et al. 2016). In contrast to the version used for the N_2O calculations described above, this version of the photochemical model incorporated additional reactions to account for the inclusion of Cl and Br chemistry. There are a total of 89 unique kinetically active chemical species and 413 reactions in this version. To compute CH_3X flux-abundance calculations, we adopted the same stellar spectra as described above for HD 85512 (K6V), Proxima Centauri (M5.5 Ve), and TRAPPIST-1 (M8V). We additionally use the M3.5 Ve star AD Leo with stellar spectra

from the Atmos library, which was ultimately sourced from (Segura et al. 2005). We do not consider G dwarf (Sun-like) or F dwarf host stars because the atmospheric accumulation of CH_3 gases is spectrally insignificant for these scenarios even at the largest plausible fluxes (Leung et al. 2022).

CH_3Cl and CH_3Br fluxes were independently and jointly co-varied according to factors of 1, 10, 100, and 1000 times the modern flux of each species. In other words, we varied: CH_3Cl while other gas fluxes are held constant (cases labeled "CH_3Cl"), CH_3Br while other gas fluxes are held constant (cases labeled "CH_3Br"), and both CH_3Cl+CH_3Br together, by the same factor based on their original Earth-like fluxes (cases labeled "CH_3X"). For more details see Appendix C, Table C2. Importantly, even the highest flux scenarios are equal to or less than the flux of these species present in productive local environments (Leung et al. 2022). As the methylation process is often an adaptation used for environmental detoxification (Jia et al. 2013), the gas fluxes produced can be directly related to the abundance of metals and metalloids in the local environment. A higher supply of substrates (Br, Cl, etc.) could generate higher fluxes. As the highest fluxes are produced at wetlands, salt marshes, and other marine/terrestrial crossover ecosystems (Tait & Moore 1995; Yang et al. 2022), a planet with greater productivity may simply require a greater percentage of these environments or accelerated weathering processes that concentrate halogens and other heavy ions (Fuge 1988). Highly productive salt marsh environments cover only .00017% of the Earth's surface, so our most productive case would only require 1.7% total surface coverage, equivalent to 5% of vegetation present today (Zhu et al. 2016; Murray et al. 2022). The actual coverage necessary may be higher or lower depending on the uniformity of production across salt marsh environments. Alternative evolutionary paths, such as widespread radiation of the methylation adaptation, could yield higher global productivity. Furthermore, the greatest atmospheric loss process is through reaction with OH, which sizably decreases in abundance for later star types (Segura et al. 2005). For targets such as TRAPPIST-1, this bestows a considerable advantage in sustaining atmospheric buildup and generating potentially detectable atmospheric features. For further discussion of methylated biosignature candidate production and accumulation, see Leung et al. (2022).

2.2. Spectral Simulations

2.2.1. PSG

Schwieterman et al. (2022) used the Planetary Spectrum Generator (PSG) to calculate the radiance (thermal emission) spectra for the Earth spectra with varying N_2O fluxes. PSG is a highly flexible and publicly available radiative tool used to simulate the remote spectral observables of planetary objects across a full range of viewing geometries and distances (Villanueva et al. 2018, 2022). PSG uses the HITRAN 2020 database for its input infrared opacities (Gordon et al. 2022). Planetary spectra were produced from 5–20 μm and are averaged 50% clear sky and 50% cloud scenarios. The clouds consisted of equal fractions of liquid water cloud and cirrus cloud particles.

2.2.2. SMART

Leung et al. (2022) used the Spectral Mapping and Radiative Transfer code (SMART; Meadows & Crisp 1996) to simulate emission spectra. This model has an extensive history of use for both the solar system and exoplanet objects and has previously

been used to simulate biosignatures such as O_2 and organic sulfur compounds (Domagal-Goldman et al. 2011; Robinson et al. 2011; Arney et al. 2014; Meadows et al. 2018b). As input, SMART uses the line-by-line absorption coefficients, which are calculated based on the HITRAN 2020 line lists (Gordon et al. 2022). For this application, 50% cloudy spectra with 25% cirrus and 25% stratocumulus clouds were modeled.

2.3. LIFESIM Observation and Population Simulations

LIFESIM is a state-of-the-art simulator software specifically designed for LIFE. As a tool, it provides accurate and reliable simulations of the interferometric measurement processes involved in the operation of LIFE. With LIFESIM, users can explore the capabilities of LIFE and gain insights into the parameter space accessible to LIFE for the detection and characterization of exoplanets.

In this work, we used two features of LIFESIM:

1. A module based on the population synthesis tool P-Pop (Kammerer & Quanz 2018) that simulates random exoplanetary systems around an input catalog of target stars based on current exoplanet statistics, e.g., from transit or radial velocity surveys. LIFEsim can then compute the detectability of each individual simulated planet and derive an optimized observing sequence for the stellar sample. This can be used to compute detection yields in the blind (target) search *detection phase* of LIFE (see Dannert et al. 2022; Kammerer et al. 2022; Quanz et al. 2022). In Section 3.1 we used this to calculate the number of potential targets available for the analysis discussed here. The assumed mission time available for the blind search phase (2.5 yr, 20% overheads) is optimally distributed among the synthetic planetary systems to optimize the number of planets detected in the habitable zone (HZ).

2. A simulator for individual spectroscopic observations in LIFE's *characterization phase* is used for the feasibility study in the following sections following the same approach as Angerhausen et al. (2023).

LIFESIM incorporates astrophysical noise sources such as stellar leakage and thermal emission from local zodiacal and exozodiacal dust. While only fundamental photon noise is considered in this study, the software is also flexible to accommodate instrumental noise terms in the future. LIFESIM offers an accessible way to predict the expected S/N of future observations based on various instrument and target parameters (see Dannert et al. 2022, for more details).

Following the same approach as in Angerhausen et al. (2023), we used LIFESIM to produce synthetic observations of the outlined exoplanet cases with different flux levels of the discussed species and also without them being present in their atmospheres. For the presented output spectra, LIFESIM is configured with the current LIFE "baseline" setup with four apertures of 2 m diameter each, a broadband wavelength range of 4–18.5 μm, a throughput of 5%, and a spectral resolution of $R = 50$. While the detection phase simulation sampled over a distribution of exozodi levels, we assume an exozodi level of 3 times the local zodi density for the characterization observations (following the results from the HOSTS survey for the expected median level of emission inErtel et al. 2020) and a nulling baseline setup between 10 and 100 m[13]

---

[13] Here, we assume that the planets are known from other surveys or detected in the LIFE detection phase so that we can optimize the baselines for each case.

Table 1
Overview of Simulation Parameters Used in LIFESIM

Parameter	Value
Quantum efficiency	0.7
Throughput	0.05
Minimum Wavelength	4 μm
Maximum Wavelength	18.5 μm
Spectral Resolution	50
Interferometric Baseline	10–100 m
Apertures Diameter	2 m
Exozodi	3× local zodi

Note. These are the same standard values as, e.g., used in Quanz et al. (2022) or Angerhausen et al. (2023).

(see Table 1). In Section 4.3 we present a short analysis of the impact that changes in this setup have for the dectectability of selected cases.

3. Results

3.1. Predicted Distance Distribution of HZ Planets Around M and FGK-type Stars Detectable with LIFE

As a first step in our study, we identify how many planets we would encounter in our survey for this analysis and at what typical distances from the solar system their host stars appear. Therefore we used the LIFESIM population part to estimate the distance distribution of HZ planets with radii between 0.5 and 1.5 $R_\odot$ around M and FGK-type stars within 20 pc of the Sun that are detectable with LIFE. For the sake of comparability to previous studies, our yield predictions were based on planet populations generated by Quanz et al. (2022) and Kammerer et al. (2022), respectively.

Hence, we note that the number of planets around M and FGK-type stars were calculated in two separate simulations, (1) optimizing the maximum yield of HZ planets in general using a synthetic planet population around a sample of AFGKM-type and (2) optimizing the number of HZ planets around FGK stars only using a subsample of FGK-type host stars within our target database (Quanz et al. 2022).

These populations were derived from two sets of rocky planet occurrence rate estimates: (1) Similar to Quanz et al. (2022), occurrence rates from NASA's ExoPaG SAG13 (Kopparapu et al. 2018) were used for AFGK-type stars with effective temperatures between 3940 and 9700 K, and results from Dressing & Charbonneau (2015) were applied to M-type stars with effective temperatures between 2440 and 3800 K. (2) As in Kammerer et al. (2022), exoplanet occurrence rate estimates from Bryson et al. (2021), based on Kepler Data Release 25 (DR25) planet catalog data (Thompson et al. 2018) and Gaia-based stellar properties (Gaia Collaboration et al. 2018), were used to compute separate planet yield predictions around a subsample of FGK-type stars with effective temperatures between 3940 and 7220 K. In comparison to estimates from NASA's ExoPaG SAG13 (Kopparapu et al. 2018), planet occurrence rates in Bryson et al. (2021) cover the entire parameter range of the optimistic HZ around early-type stars. Here, we used the *model 1 hab2 stars high bound* scenario from Bryson et al. (2021). We focused on model 1 because it considers more parameters to model the underlying planet population, including the stellar effective temperature. Moreover, the hab2 stars sample is based on a larger number of
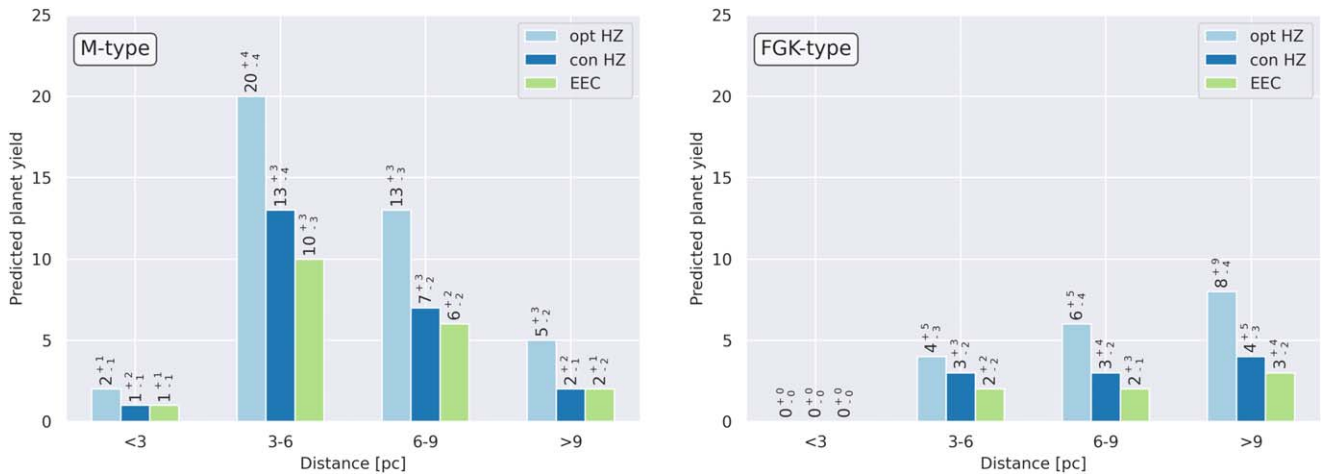
Figure 1. Distance distribution of HZ planet populations around M and FGK-type stars detectable with LIFE in the current baseline setup (see Table 1). Left: Detection yield predictions for planets around M-type stars with an underlying AFGKM exoplanet population following occurrence rate estimates from NASA's ExoPaG SAG13 (Kopparapu et al. 2018) and Dressing & Charbonneau (2015). Right: Detection yields predictions around FGK-type stars with an underlying FGK exoplanet population based on the occurrence rates from Bryson et al. (2021). We differentiate between three HZ definitions: optimistic (opt) HZ, conservative (con) HZ, and EECs. The bars show the predicted median planet yields and 1σ uncertainties derived from the Monte Carlo simulations.

planet candidates and a wider range of stellar effective temperatures. Finally, the high bound is considering a more optimistic extrapolation of the Kepler occurrence rates beyond orbital periods of 500 days for which completeness characterization is not available in Kepler DR25 (Thompson et al. 2018), in which the completeness beyond 500 days is assumed to be zero. For further details about the planet occurrence rate model, we refer the reader to Bryson et al. (2021). Based on these occurrence rates, (1) 500 and (2) 1000 synthetic planet populations were generated around each star in our target sample (Quanz et al. 2022) with the population synthesis tool P-Pop (Kammerer & Quanz 2018). We associated all planetary systems with circular orbits which were uniformly distributed on the sphere. A multiplanet stability criterion was assumed to have a negligible impact on the derived yield estimates. For further details see Kammerer et al. (2022). By averaging over a multitude of Monte Carlo realizations, we marginalized over different population properties such as the number of planets per simulated universe, exozodiacal dust levels, and orbital parameters, and with this, we are able to account for uncertainties in the underlying occurrence rate model.

For retrieving the integration time required to detect each planet in the synthetic planet populations, we simulated photon noise from all major astrophysical noise sources with the observation simulation tool LIFESIM (Dannert et al. 2022). The observation time was distributed such that the number of planets in the HZ around their respective host stars was optimized. As instrumental noise is not considered in the current implementation of LIFESIM (F. Dannert et al. 2024, in preparation), we assumed a conservatively high signal-to-noise ratio (S/N) of 7 integrated over the full wavelength range, partly to also leave some margin for currently unaccounted instrumental errors. We assigned each planetary system an exozodiacal dust level randomly drawn from the nominal exozodi level distribution with a median of ∼3 zodi according to results from the HOSTS survey (Ertel et al. 2018, 2020). As Kammerer et al. (2022) previously showed the planet yield to be largely independent of the interferometric baseline length optimization scheme, we chose a baseline length optimization for the center of the optimistic HZ. We assumed a reference implementation of LIFE mission parameters corresponding to

Table 2
Modeled S/N Ratios for Various Intergration Times and Different Fluxes of N_2O at a 5 Pc Sun-like Star

T_{int} (day)	Feature	Band-int. S/N	Max. Line Sigma
10	1 Tmol yr^{-1} N_2O	0.7	0.4
10	10 Tmol yr^{-1} N_2O	2.3	1.2
10	100 Tmol yr^{-1} N_2O	6.6	3.3
50	1 Tmol yr^{-1} N_2O	1.5	0.9
50	10 Tmol yr^{-1} N_2O	5.1	2.7
50	100 Tmol yr^{-1} N_2O	14.7	7.5
100	1 Tmol yr^{-1} N_2O	2.1	1.3
100	10 Tmol yr^{-1} N_2O	7.2	3.8
100	100 Tmol yr^{-1} N_2O	20.7	10.6

an aperture size of $D = 2$ m, throughput of 5%, and a wavelength coverage of $\lambda = 4$–18.5 μm. Other adopted mission specifications correspond to the descriptions in Quanz et al. (2022). We compared predicted planet yields for three different HZ definitions: planets located within the optimistic HZ, within the conservative HZ, and exo-Earth candidates (EEC). For incident stellar flux and planetary radii limits of the respective HZ models see Kopparapu et al. (2014) and Stark et al. (2019). The derived distance distributions of detectable HZ planets around M and FGK-type stars are shown in Figure 1.

In summary, we find that we will have a typical sample of 15–20 HZ planets at distances less than 6 pc. This motivates and justifies the choice of our examples at 5 pc. These would be the typical distance for HZ planets around late-type stars and the case for a few best targets around earlier types.

3.2. Detectability of N_2O

We modeled the detectability of N_2O for a set of observation times of 10, 50, and 100 days using the LIFE baseline setup shown in Table 1. Based on our experience from previous LIFE studies (e.g., Alei et al. 2022b; Konrad et al. 2022; Angerhausen et al. 2023) the 10 day case represents a relatively short (potentially preliminary) characterization observation that can be conducted for a larger sample of targets, 50 days represent a
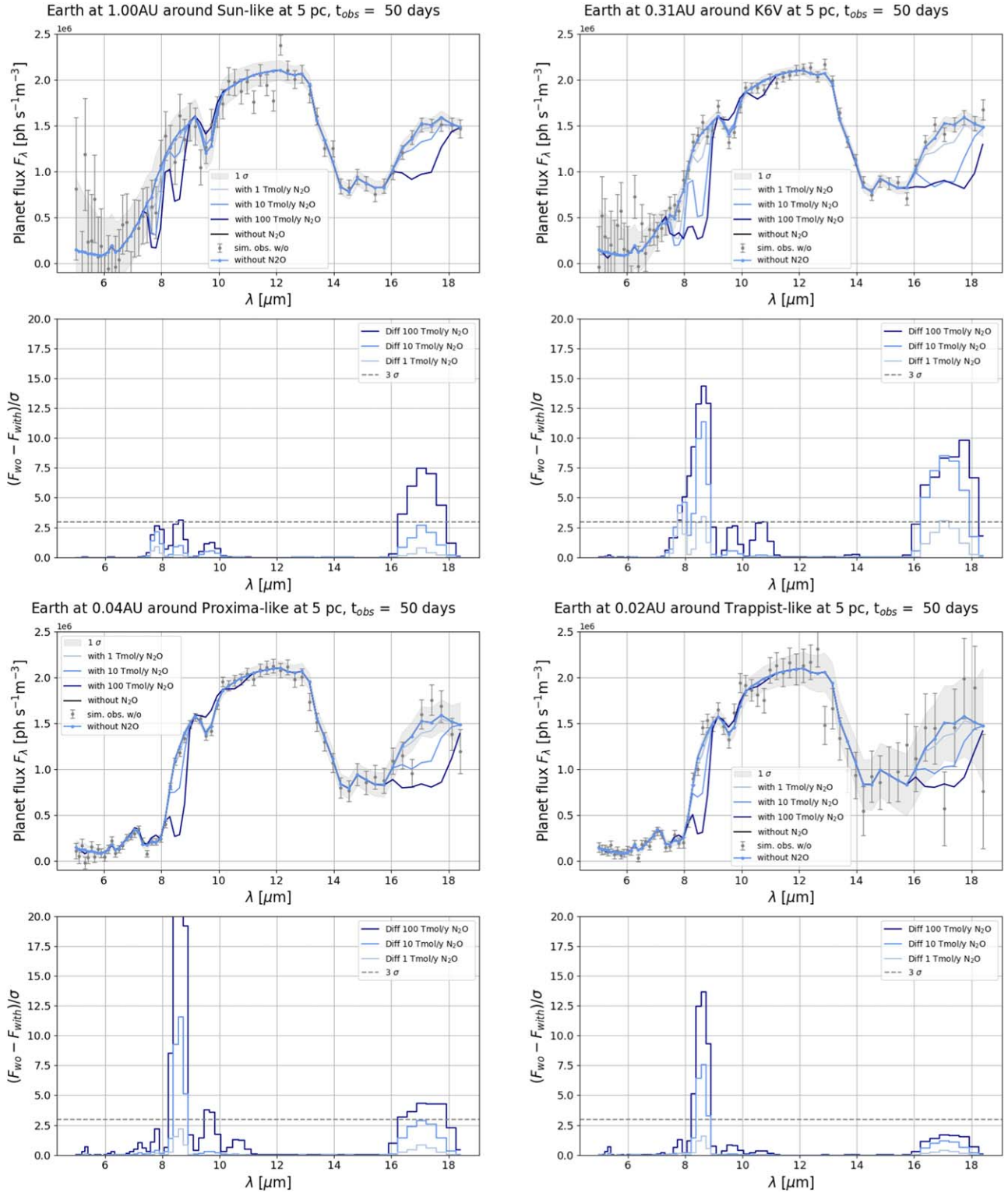
Figure 2. Detectability of various fluxes of N_2O in the emission spectrum of an Earth-like planet around a (from top left to bottom right:) Sun-like, K6V, Proxima Centauri-type, and Trappist-like star at 5 pc, after 50 days of observation with LIFE. Top: planet flux for atmospheres with and without N_2O. The gray area represents the 1σ sensitivity; the dark gray error bars show an individual simulated observation. Bottom: Statistical significance of the detected differences between atmospheric models with and without N_2O. For the Sun-like case, the main contribution to the detectability is in the 16–18 μm band. For the later-type star cases, the differences are especially in the 8–9 μm band (see also the discussion in Section 4.1).

more thorough observation and 100 days will be the deepest characterization observation for only the most interesting/promising targets for LIFE. In Section 4.3 we also vary the integration times and explore setups beyond the LIFE baseline. It is worthwhile to mention that these numbers may correspond to

a significant fraction of the orbital periods of the considered planets, and in some cases they even clearly exceed them. Here we assume that the planet signal is stationary in LIFESIM and that we can add the signal of multiple visits without significantly increasing the noise contributions.

Table 3
Modeled S/N Ratios for Various Integration Times and Different Fluxes of
N_2O at a 5 Pc Proxima Centauri–like Star

T_{int} (day)	Feature	Band-int. S/N	Max. Line Sigma
10	1 Tmol yr^{-1} N_2O	1.3	1.0
10	10 Tmol yr^{-1} N_2O	7.4	5.2
10	100 Tmol yr^{-1} N_2O	18.3	11.1
50	1 Tmol yr^{-1} N_2O	3.0	2.2
50	10 Tmol yr^{-1} N_2O	16.5	11.6
50	100 Tmol yr^{-1} N_2O	40.9	24.8
100	1 Tmol yr^{-1} N_2O	4.3	3.0
100	10 Tmol yr^{-1} N_2O	23.4	16.4
100	100 Tmol yr^{-1} N_2O	57.9	35.0

Table 4
Modeled S/N Ratios for Various Integration Times and Different Fluxes of
N_2O at a 5 pc K6V Star

T_{int} (day)	Feature	Band-int. S/N	Max. Line Sigma
10	1 Tmol yr^{-1} N_2O	3.6	1.7
10	10 Tmol yr^{-1} N_2O	10.8	5.1
10	100 Tmol yr^{-1} N_2O	15.0	6.4
50	1 Tmol yr^{-1} N_2O	8.1	3.7
50	10 Tmol yr^{-1} N_2O	24.1	11.4
50	100 Tmol yr^{-1} N_2O	33.6	14.3
100	1 Tmol yr^{-1} N_2O	11.5	5.3
100	10 Tmol yr^{-1} N_2O	34.1	16.1
100	100 Tmol yr^{-1} N_2O	47.5	20.3

Table 5
Modeled S/N Ratios for Various Integration Times and Different Fluxes of
N_2O at a 5 pc TRAPPIST-1 Like Star

T_{int} (day)	Feature	Band-int. S/N	Max. Line Sigma
10	1 Tmol yr^{-1} N_2O	0.9	0.7
10	10 Tmol yr^{-1} N_2O	4.8	3.4
10	100 Tmol yr^{-1} N_2O	9.7	6.1
50	1 Tmol yr^{-1} N_2O	2.1	1.6
50	10 Tmol yr^{-1} N_2O	10.8	7.6
50	100 Tmol yr^{-1} N_2O	21.8	13.7
100	1 Tmol yr^{-1} N_2O	3.0	2.2
100	10 Tmol yr^{-1} N_2O	15.2	10.7
100	100 Tmol yr^{-1} N_2O	30.8	19.3

Table 6
Modeled S/N Ratios for Various Integration Times and Different Fluxes of
CH3X Around a Proxima Centauri-type Host at 5 pc

T_{int} (day)	Feature	Band-int. S/N	Max. Line Sigma
10	1× CH_3X	0.8	0.5
10	10× CH_3X	6.9	3.1
10	100× CH_3X	21.0	8.7
10	1× CH_3Cl	1.6	1.2
10	10× CH_3Cl	3.4	2.0
10	100× CH_3Cl	11.5	5.1
10	1× CH_3Br	0.5	0.2
10	10× CH_3Br	2.4	1.2
10	100× CH_3Br	6.4	3.2
50	1× CH_3X	1.9	1.1
50	10× CH_3X	15.4	7.0
50	100× CH_3X	46.9	19.5
50	1× CH_3Cl	3.6	2.6
50	10× CH_3Cl	7.6	4.6
50	100× CH_3Cl	25.8	11.5
50	1× CH_3Br	1.1	0.5
50	10× CH_3Br	5.3	2.7
50	100× CH_3Br	14.4	7.1
100	1× CH_3X	2.7	1.6
100	10× CH_3X	21.8	9.9
100	100× CH_3X	66.3	27.6
100	1× CH_3Cl	5.1	3.7
100	10× CH_3Cl	10.8	6.4
100	100× CH_3Cl	36.5	16.2
100	1× CH_3Br	1.6	0.7
100	10× CH_3Br	7.5	3.8
100	100× CH_3Br	20.3	10.1

For all simulated observations we calculated two metrics for the detectability of the discussed cases: the maximum difference in a single spectral line (usually in the absorption band of the feature in question) in units of the respective sensitivity in that channel and a bandpass-integrated S/N defined as

$$S/N = \sqrt{\Sigma_{i=1}^{n}\left(\frac{\Delta y_i}{\sigma(y_i)}\right)^2},$$

where Δy_i is the difference between the two spectra (one spectrum containing the species and the other that does not) in each of the n spectral bins and $\sigma(y_i)$ is the LIFE sensitivity the respective bin. This assumes independence between the bins and was used in a similar manner in, e.g., Lustig-Yaeger et al. (2019) or Bixel & Apai (2021). As a rule of thumb, we assume a case is observable (i.e., the feature is distinguishable) if the band-integrated S/N is above 5–10 and the single line sigma above 3 (more on the justification of these numbers in Section 3.4, where we compare those to some exemplary full retrievals).

3.2.1. Sun-like G Star

The results for an Earth-like planet orbiting a Sun-like star at 5 pc distance are listed in Table 2 and shown in Figure 2 for a 50 day observation (more cases for 10 and 100 days are shown in Appendix B.1 Figures B1 and B2). In these figures (also for the other N_2O cases in Sections 3.2.2 to 3.2.4), the top panel shows the planet flux for atmospheres with and without N_2O and the gray area represents the 1σ sensitivity calculated with LIFEsim while the dark gray error bars show an individual simulated observation. The bottom panel analyses the statistical significance of the detected differences between atmospheric models with and without N_2O. Our analysis shows that the 100 Tmol yr^{-1} case is likely observable already after 10 days (with S/N of 6.6/3.3 in our two metrics), while the 10 Tmol yr^{-1} model seems to become observable around or slightly after day 50. The 1 Tmol yr^{-1} is beyond our sensitivity, only reaching S/Ns of 2.1/1.3 even for integration times of 100 days. Noteworthy here is that this detection is driven by the longer (16–18 μm) wavelength bands of N_2O.
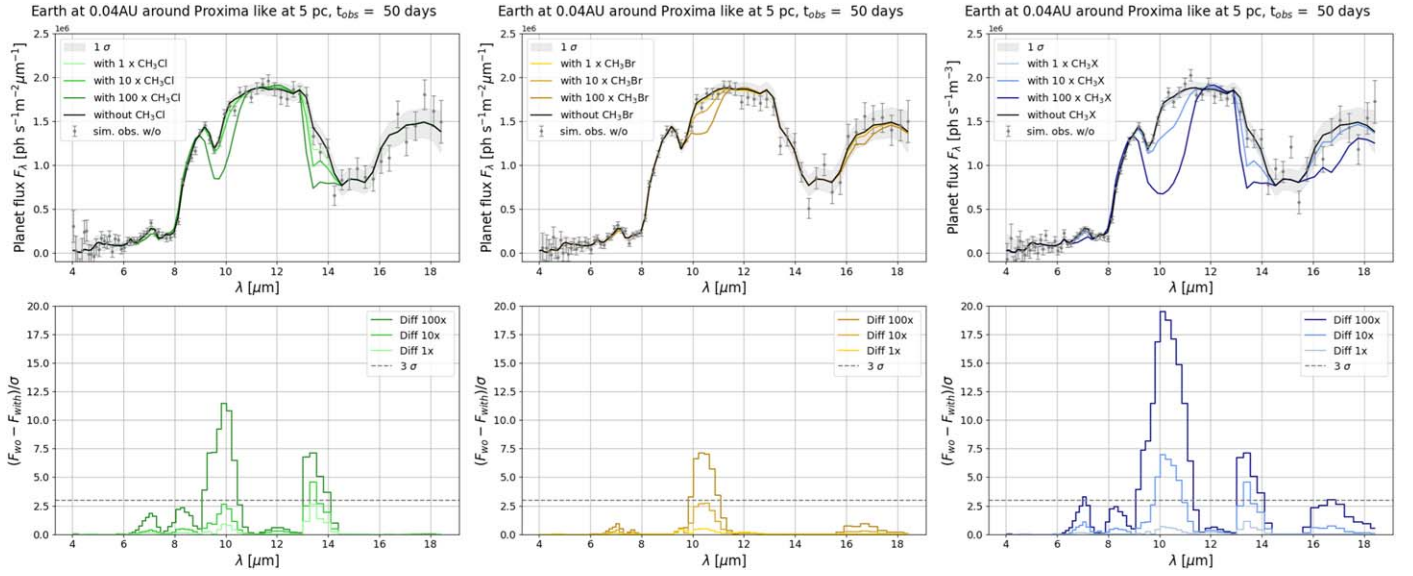
Figure 3. Detectability of various levels of CH_3Cl and CH_3Br fluxes in the emission spectrum of an Earth-like planet around a Proxima Centauri-type star, after 50 days of observation with LIFE. Top: planet flux for atmospheres with and without CH_3Cl and CH_3Br. The gray area represents the 1σ sensitivity; the gray error bars show an individual simulated observation. Bottom: Statistical significance of the detected differences between an atmospheric model with and without CH_3Cl and CH_3Br.

Table 7
Modeled S/N Ratios for Various Integration Times and Different Fluxes of CH3X Around an AD Leonis–type Host at 5 pc

T_{int} (day)	Feature	Band-int. S/N	Max. Line Sigma
10	$1\times CH_3X$	0.8	0.4
10	$10\times CH_3X$	3.1	2.3
10	$100\times CH_3X$	9.8	4.6
10	$1\times CH_3Cl$	0.8	0.4
10	$10\times CH_3Cl$	3.1	2.3
10	$100\times CH_3Cl$	8.7	4.6
10	$1\times CH_3Br$	0.7	0.4
10	$10\times CH_3Br$	0.7	0.4
10	$100\times CH_3Br$	2.0	1.0
50	$1\times CH_3X$	1.8	1.0
50	$10\times CH_3X$	7.0	5.1
50	$100\times CH_3X$	21.8	10.2
50	$1\times CH_3Cl$	1.8	1.0
50	$10\times CH_3Cl$	6.9	5.1
50	$100\times CH_3Cl$	19.4	10.2
50	$1\times CH_3Br$	1.5	0.8
50	$10\times CH_3Br$	1.6	0.8
50	$100\times CH_3Br$	4.5	2.3
100	$1\times CH_3X$	2.5	1.4
100	$10\times CH_3X$	9.9	7.2
100	$100\times CH_3X$	30.9	14.4
100	$1\times CH_3Cl$	2.5	1.4
100	$10\times CH_3Cl$	9.7	7.2
100	$100\times CH_3Cl$	27.4	14.4
100	$1\times CH_3Br$	2.1	1.2
100	$10\times CH_3Br$	2.2	1.2
100	$100\times CH_3Br$	6.4	3.2

This prototypical science case of an Earth-twin scenario with these additional fluxes will be discussed in more detail in Sections 3.4 and 4.3 where we use these for exemplary retrievals and derive consequences for the current mission design in the context of science and technology requirements.

3.2.2. Proxima Centauri-type Star

The results for an Earth-like planet orbiting a M5.5 Ve Proxima Centauri-type star at 5 pc distance are listed in Table 3 and shown in Figure 2 for a 50 day observation (more cases simulating 10 and 100 days of integration time shown in Appendix B.1, Figures B1 and B2). In Section 4.2, we discuss the case of a planet orbiting Proxima Centauri at its actual distance of 1.3 pc as an example of a "golden target" that allows for very detailed, potentially even time resolved LIFE observations. For this scenario, the 100 as well as the 10 Tmol yr^{-1} case are detectable in the 10 days simulations with S/Ns consistently above 5, while the 1 Tmol yr^{-1} seems to only barely touch the detection threshold after 100 days (with S/Ns of 4.3/3.0). This case is one of the best observable ones in this study. In comparison to the previous case, here the shorter (8–10 μm) wavelength bands of N_2O contribute the most to the band-integrated S/N (see Section 4.1).

3.2.3. K6V

The results for an Earth-like planet orbiting a K6V star at 5 pc distance are listed in Table 4 and shown in Figure 2 for a 50 day observation (more cases simulating 10 and 100 days of integration time are shown in Appendix B.1, Figures B1 and B2). The results are very similar to and even slightly more significant than the Proxima Centauri-type case. Once again, the 100 and 10 Tmol yr^{-1} cases are detectable in the 10 day simulations, reaching S/N of over 10/5 in our two metrics. The 1 Tmol yr^{-1} case crosses the detection threshold with an S/N of 8.1/3.7 at around 50 days.

3.2.4. TRAPPIST-1 Like Star

The results for an Earth-like planet orbiting a TRAPPIST-1 like star at 5 pc distance are listed in Table 5 and shown in Figure 2 for a 50 day observation (more cases simulating 10 and 100 days of integration time are shown in Appendix B.1, Figures B1 and B2). Similar to the above cases for the K6V and
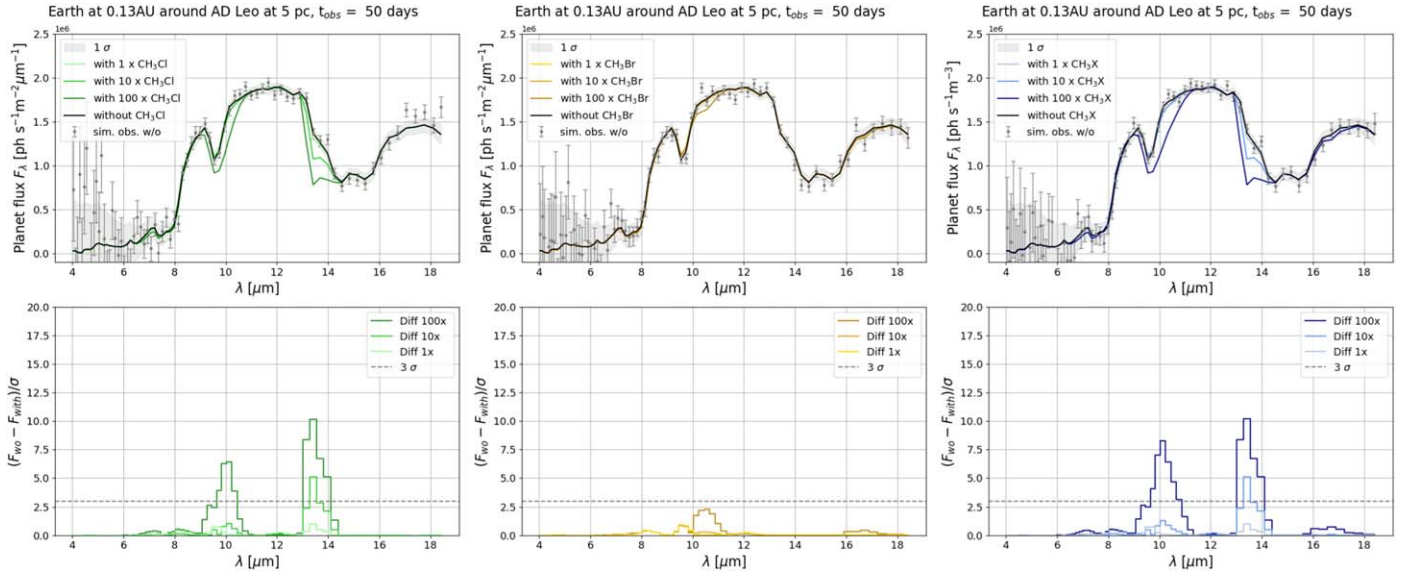
Figure 4. Detectability of various levels of CH_3Cl and CH_3Br fluxes in the emission spectrum of an Earth-like planet around an AD Leonis–type star, after 50 days of observation with LIFE. Top: planet flux for atmospheres with and without CH_3Cl and CH_3Br. The gray area represents the 1σ sensitivity; the gray error bars show an individual simulated observation. Bottom: Statistical significance of the detected differences between an atmospheric model with and without CH_3Cl and CH_3Br.

Proxima Centauri-type host stars, the 100 and 10 Tmol yr^{-1} cases cross the detection threshold in the 10 day simulations with the S/N metrics at 4.8/9.7 and 3.4/6.1, respectively. The 1 Tmol yr^{-1} case only seems on the edge of detectability even after 100 days reaching band-integrated S/N of 3.0.

3.3. Detectability of CH_3X

Similarly to the N_2O cases discussed in the last section, we modeled the detectability of CH_3X for a set of observation times of 10 days, 50 days and 100 days. Again, we used the two metrics for the detectability introduced above: a maximum difference in a single line in units of the respective sensitivity in that channel and a bandpass-integrated S/N.

3.3.1. Proxima Centauri-type Star

The results for an Earth-like planet orbiting a Proxima Centauri (M5.5 Ve)–type star at 5 pc distance from the Sun are listed in Table 6 and shown in Figure 3 for a 50 day observation (modeled observations of 10 and 100 days are shown in Appendix B.2, Figures B3–B4). After 10 days, the 100× and 10× CH_3X and 100× CH_3Cl cases are detectable with S/Ns above 10/5 in the two metrics used here. After 50 days the 100× CH_3Br case becomes detectable, reaching S/Ns of 14.4/7.1. After 100 days all the 1× cases are still below our detectability limit, while all the 10× and 100× cases seem detectable.

3.3.2. AD Leonis–type star

The results for an Earth-like planet orbiting an AD Leonis–type M3.5V star at 5 pc distance from the Sun are listed in Table 7 and shown in Figure 4 for a 50 day observation (more cases for 10 and 100 day observations are shown in Appendix B.2, Figures B5–B6). In this scenario only the 100× and (as this case is dominated by CH_3Cl) 100× cases are detectable after 10 days with S/Ns of 9.8/4.6 and 8.7/4.6. It would, however, take more than 50 and up to 100 days in the LIFE baseline setup to make the various 10× cases

Table 8
Modeled S/N Ratios for Various Integration Times and Different Fluxes of CH3X Around a K6V Star at 5 pc

T_{int} (day)	Feature	Band-int. S/N	Max. Line Sigma
10	1× CH_3X	0.2	0.1
10	10× CH_3X	0.4	0.3
10	100× CH_3X	2.5	1.6
10	1× CH_3Cl	2.1	1.1
10	10× CH_3Cl	0.4	0.3
10	100× CH_3Cl	2.4	1.5
10	1× CH_3Br	0.2	0.1
10	10× CH_3Br	0.3	0.2
10	100× CH_3Br	1.4	1.0
50	1× CH_3X	0.5	0.3
50	10× CH_3X	0.8	0.6
50	100× CH_3X	5.5	3.5
50	1× CH_3Cl	4.6	2.5
50	10× CH_3Cl	0.9	0.6
50	100× CH_3Cl	5.4	3.4
50	1× CH_3Br	0.5	0.3
50	10× CH_3Br	0.8	0.5
50	100× CH_3Br	3.1	2.1
100	1× CH_3X	0.7	0.4
100	10× CH_3X	1.1	0.9
100	100× CH_3X	7.8	4.9
100	1× CH_3Cl	6.5	3.5
100	10× CH_3Cl	1.2	0.9
100	100× CH_3Cl	7.7	4.8
100	1× CH_3Br	0.7	0.4
100	10× CH_3Br	1.1	0.8
100	100× CH_3Br	4.4	3.0

observable. All of the cases with 1× and the 10× CH_3Br case do not cross the threshold of detectability even after 100 days.

3.3.3. K6V-type Star

The results for an Earth-like planet orbiting a K6V-type star at 5 pc distance from the Sun are listed in Table 8 and shown in
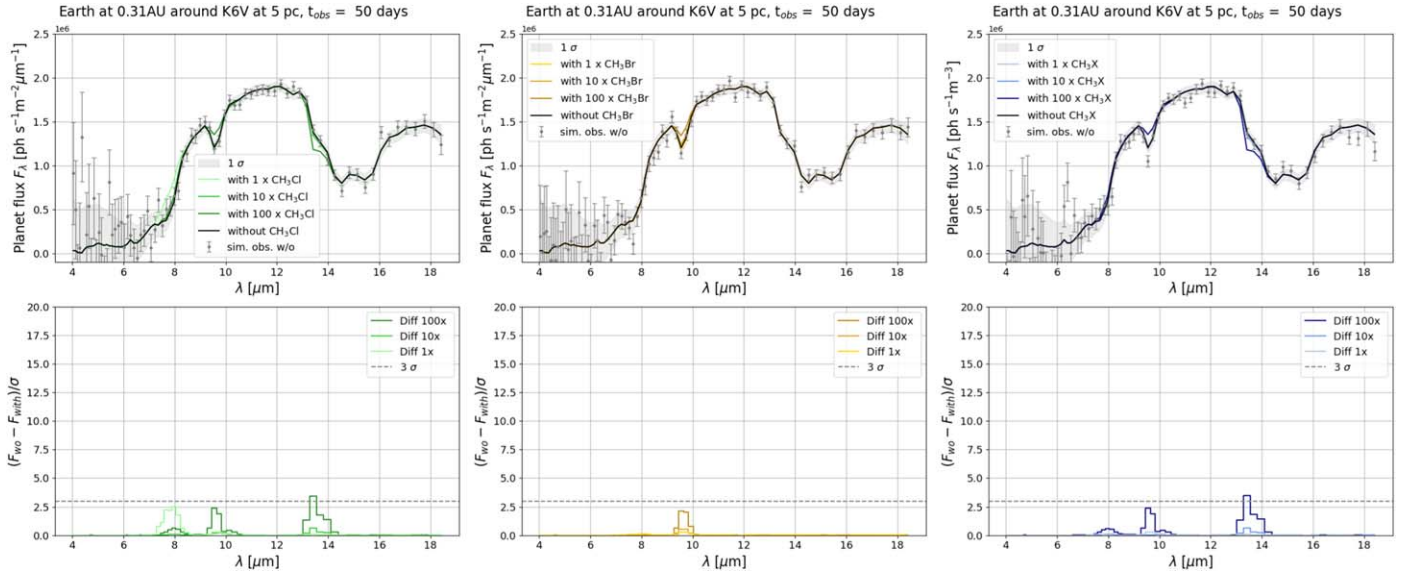
Figure 5. Detectability of various levels of CH₃Cl and CH₃Br fluxes in the emission spectrum of an Earth-like planet around a K6V-type star, after 50 days of observation with LIFE. Top: planet flux for atmospheres with and without CH₃Cl and CH₃Br. The gray area represents the 1σ sensitivity; the gray error bars show an individual simulated observation. Bottom: Statistical significance of the detected differences between an atmospheric model with and without CH₃Cl and CH₃Br. None of these cases seem to be detectable.

Table 9
Modeled S/N Ratios for Various Integration Times and Different Fluxes of CH3X Around a TRAPPIST-like Star at 5 pc

T_{int} (day)	Feature	Band-int. S/N	Max. Line Sigma
10	$1\times$ CH₃X	0.7	0.4
10	$10\times$ CH₃X	4.6	2.1
10	$100\times$ CH₃X	9.3	4.0
10	$1\times$ CH₃Cl	0.6	0.4
10	$10\times$ CH₃Cl	1.7	0.9
10	$100\times$ CH₃Cl	5.3	2.3
10	$1\times$ CH₃Br	0.5	0.2
10	$10\times$ CH₃Br	1.1	0.5
10	$100\times$ CH₃Br	2.2	1.1
50	$1\times$ CH₃X	1.5	0.8
50	$10\times$ CH₃X	10.3	4.7
50	$100\times$ CH₃X	20.8	8.9
50	$1\times$ CH₃Cl	1.5	0.8
50	$10\times$ CH₃Cl	3.9	2.1
50	$100\times$ CH₃Cl	11.8	5.2
50	$1\times$ CH₃Br	1.2	0.5
50	$10\times$ CH₃Br	2.4	1.2
50	$100\times$ CH₃Br	5.0	2.5
100	$1\times$ CH₃X	2.2	1.2
100	$10\times$ CH₃X	14.6	6.7
100	$100\times$ CH₃X	29.5	12.5
100	$1\times$ CH₃Cl	2.1	1.2
100	$10\times$ CH₃Cl	5.5	2.9
100	$100\times$ CH₃Cl	16.7	7.3
100	$1\times$ CH₃Br	1.7	0.7
100	$10\times$ CH₃Br	3.4	1.6
100	$100\times$ CH₃Br	7.0	3.5

Figure 5 for a 50 day observation (more cases shown in Appendix B.2, Figures B7–B8). This is the least favorable case discussed in this paper and almost none of the cases seem to be observable. Only for $100\times$ CH₃X and $100\times$ CH₃Cl after 100 days of observation do we barely cross the detection threshold with our S/N metrics at 7.8 and 4.9, respectively.

3.3.4. TRAPPIST-1 type star

The results for an Earth-like planet orbiting a TRAPPIST-1 type star at 5 pc distance from the Sun are listed in Table 9 and shown in Figure 6 for a 50 day observation (more cases for 10 and 100 days of observation are shown in Appendix B.2, Figures B9–B10). For this case, the $100\times$ CH₃X case is detectable with S/Ns of 9.3/4.0 already after 10 days. The $10\times$ CH₃X (10.3/4.7) as well as the $100\times$ CH₃Cl (11.8/5.2) become detectable after 50 days. Even after 100 days of simulated observation, all $1\times$ cases and the $10\times$ CH₃Cl and CH₃Br remain undetectable.

3.4. Comparison to Full Spectral Retrievals

In order to benchmark the results of the previously presented exercise of comparing spectra with and without the species present in the atmosphere, we performed a few exemplary retrievals. This was done in the following manner: the input spectra were produced as described in the sections above while our retrievals were performed with the retrieval suite described in Konrad et al. (2022) and Alei et al. (2022b). The retrieval routine couples the forward model *petitRADTRANS* (Mollière et al. 2019) with the parameter estimation module *pyMultiNest* (Buchner et al. 2014). The retrieval routine—in contrast to the forward models used for the input spetra—neglected clouds and assumed pressure-constant abundance profiles for every species included in the calculation. The spectral calculation within the retrieval was performed considering HITRAN 2020 opacities, assuming air broadening and a line wing cutoff at $25\,\text{cm}^{-1}$ from the line core.

As shown in Alei et al. (2022b), neglecting clouds in retrievals when considering spectra of partly cloudy planets is overall not impacting a correct retrieval of the chemical composition of the atmosphere. However, the opacity line lists used in the retrievals are generally not consistent with the line lists used by PSG and SMART that produced the input spectra. As discussed in Alei et al. (2022a), differences in opacities might cause considerable differences in retrievals. Other
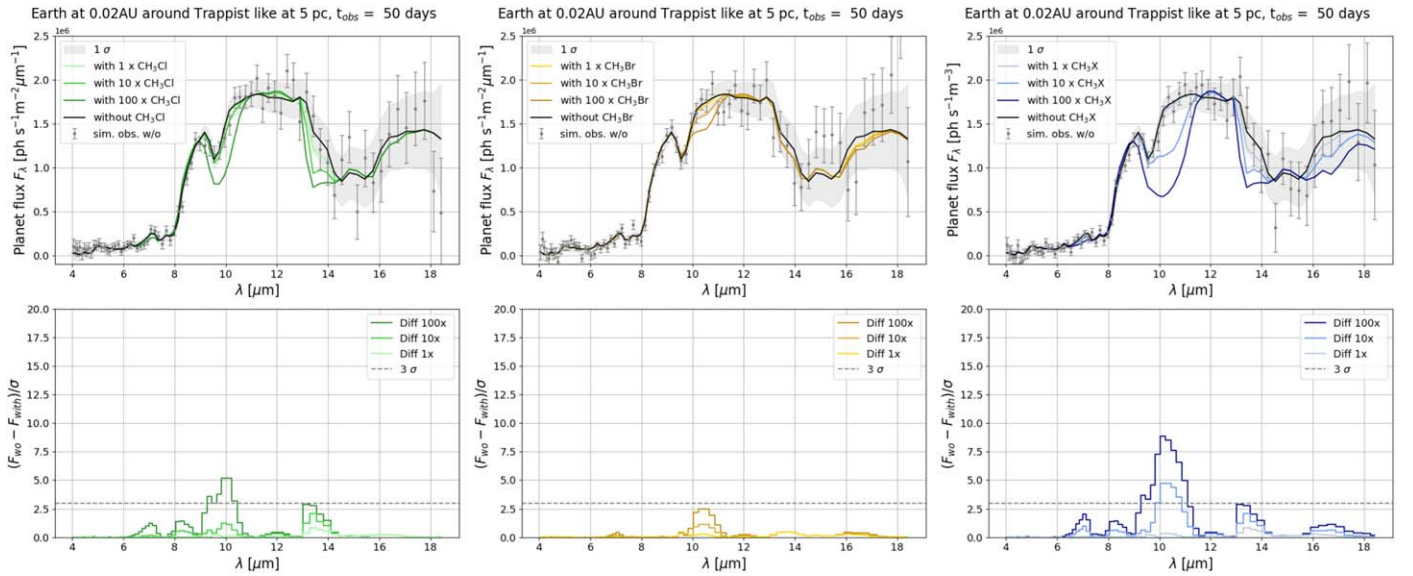
Figure 6. Detectability of various levels of CH_3Cl and CH_3Br fluxes in the emission spectrum of an Earth-like planet around a TRAPPIST-1 type star, after 50 days of observation with LIFE. Top: planet flux for atmospheres with and without CH_3Cl and CH_3Br. The gray area represents the 1σ sensitivity; the gray error bars show an individual simulated observation. Bottom: Statistical significance of the detected differences between an atmospheric model with and without CH_3Cl and CH_3Br.
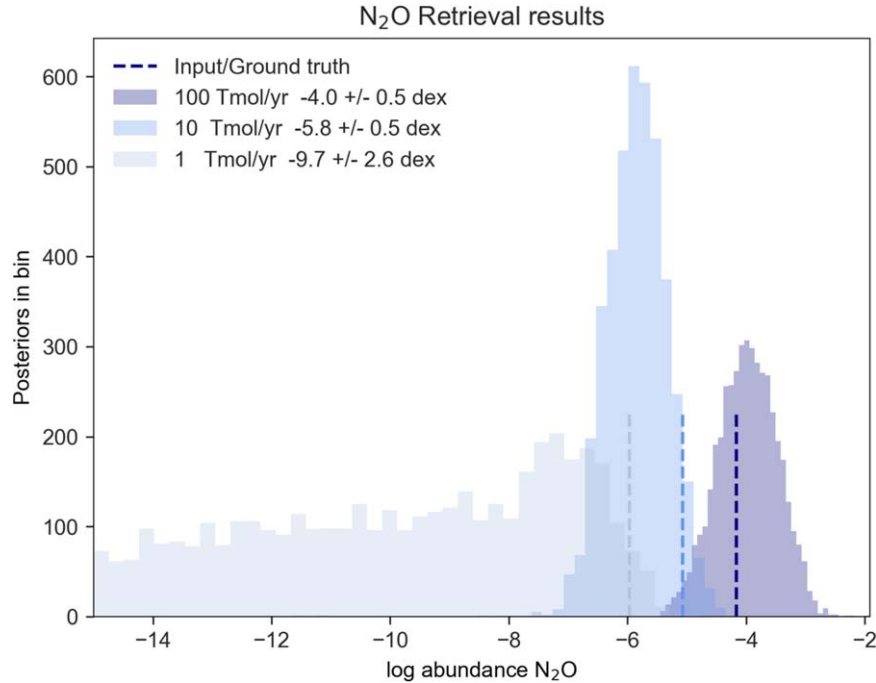
Figure 7. Comparison—Retrieval. Histograms of the posterior distributions for N_2O abundances in the three retrieval cases compared to the "ground truth" model values. While the 100 and 10 Tmol yr^{-1} cases are retrieved within $\sim 1.5\sigma$, the 1 Tmol yr^{-1} case only produces an upper limit. Biases seen here can be largely attributed to a degeneracy between abundances (in particular H_2O and N_2O), as shown in the corner plots in Appendix Section A.

differences in the implementation of scattering and raytracing methods might also generate biases. For this reason, an intercomparison among these three forward models (as well as other ones) has been ongoing within the community (G. Villanueva et al. 2024, in preparation) within the Climates Using Interactive Suites of Intercomparisons Nested for Exoplanet Studies (CUISINES) sponsored by the Nexus for Exoplanet System Science (NExSS).

Besides relaying the most basic system parameters (such as the distance of the system and the stellar type of the host), this was done without any other prior knowledge of the atmosphere

or about the process of generating the model spectra. This experimental setup reproduces the circumstances of an actual observation very well, in which case we also would not know any of the true values a priori.

The main question we asked was for which cases (i.e., which levels of band-integrated/max line S/N) we would get a detection and/or upper limits for the presence of the species of interest.

As an example, we chose the N_2O Earth at 5 pc around Sun-like star 50d cases and ran retrievals on the spectra for 1, 10, and 100 Tmol yr^{-1} fluxes of N_2O. In the direct comparison
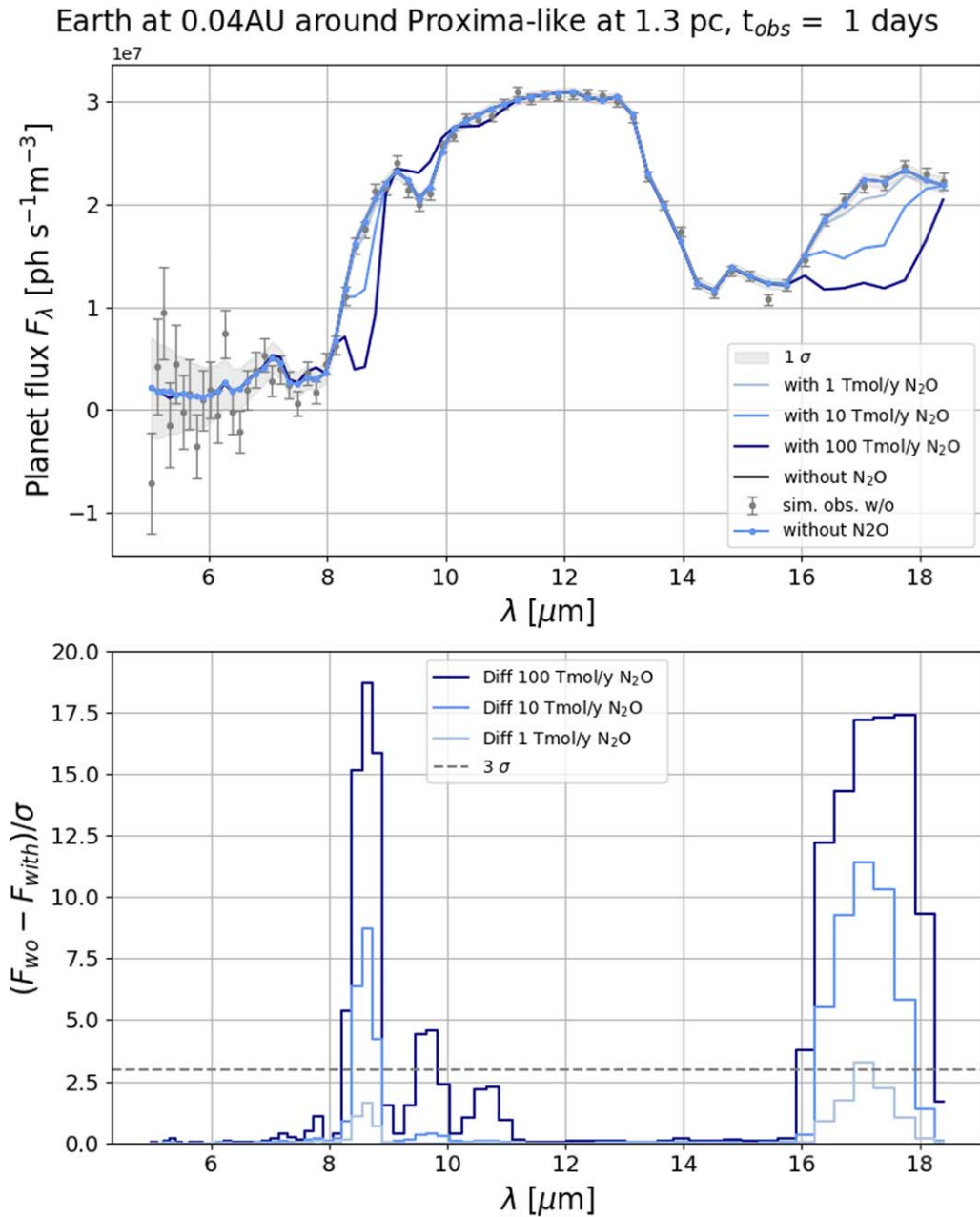
Figure 8. Detectability of various fluxes of N_2O in the emission spectrum of an Earth-like planet around Proxima Centauri at its original distance, after only 1 day of observation with LIFE. Top: planet flux for atmospheres with and without N_2O. The gray area represents the 1σ sensitivity; the dark gray error bars show an individual simulated observation. Bottom: Statistical significance of the detected differences between an atmospheric model with and without N_2O.

analysis above, these slightly more challenging cases were distinguishable from a no-N_2O case at band-integrated S/Ns of about 1.5, 5.1, and 14.7 (max. channel S/N of 0.9, 2.7, 7.5). This gives us the opportunity to compare our ability to retrieve the N_2O abundances to 1 order of magnitude in our S/N metric, giving a first-order estimate of the detection threshold in that metric. Furthermore, it connects this study with Konrad et al. (2022) and Alei et al. (2022b), who also focused on Sun-like hosts in their studies of Earth-twins.

The results are shown in Figure 7, where we show the histograms of the posteriors for the N_2O abundances for the different cases, in comparison to the "ground truth" of the input spectra. All our retrievals derive N_2O abundances within 1.5 sigma of the input value of the original models run through the LIFE observation simulator. For the 1 Tmol yr^{-1} case we

can only retrieve an upper limit. More details for the retrievals (Tables A1–A3), such as corner plots (Figures A1–A3) and values for all retrieved parameters are presented in Appendix A.

This analysis confirms our first-order estimate that a band-integrated S/N of about 5–10 should be sufficient to detect the feature in question and justifies our choice of this line as a rational, rather pessimistic detection limit in our reasoning.

4. Discussion and Conclusions

4.1. Wavelength Dependent Sensitivity Between Different Cases

In our simulations, the sensitivity of the interferometric measurement is fundamentally limited by astrophysical noise
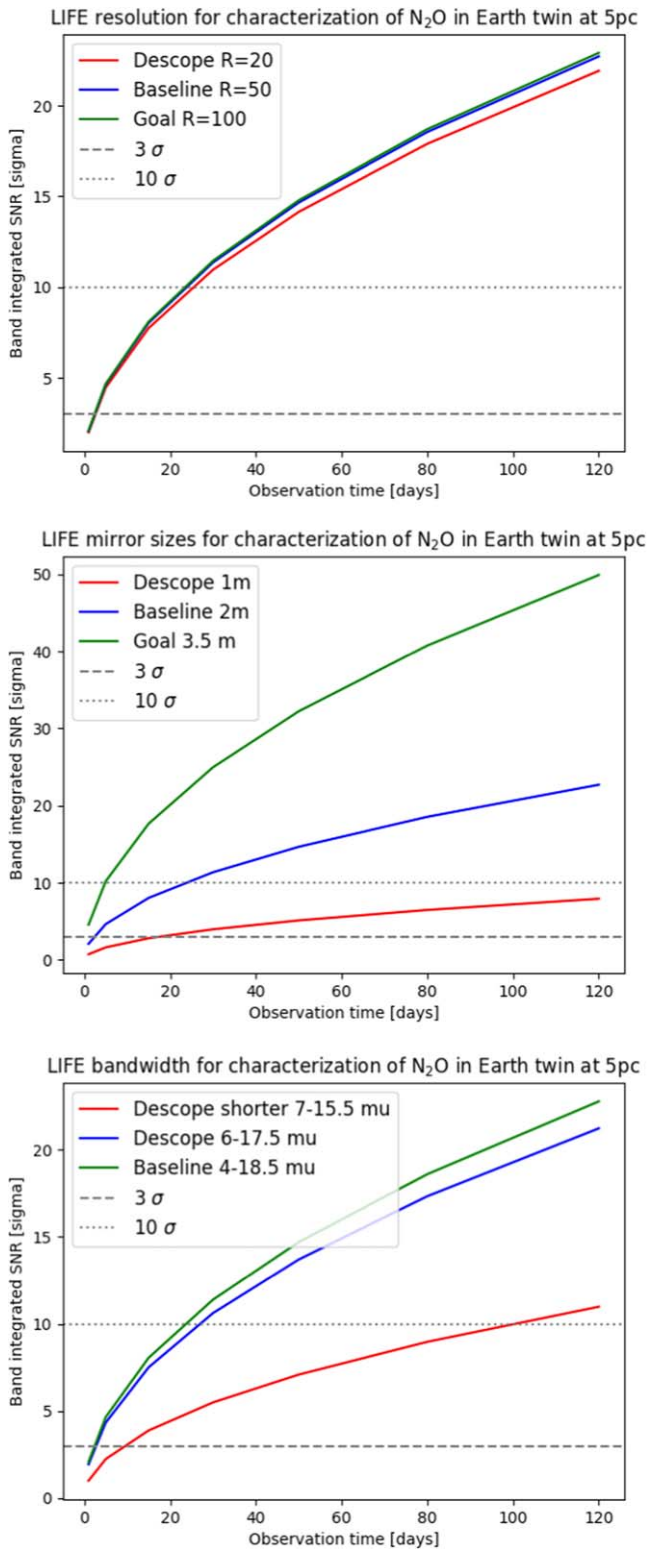
Figure 9. Dependence of observation time needed to detect 10 Tmol yr^{-1} N$_2$O in the Earth twin around Sun-like star at 5 pc example case on various mission parameters.

sources. In the longer wavelength regime of the simulated measurement, this astrophysical noise is dominated by the thermal emission of the local zodiacal dust in the solar system. The diffuse nature of the emission makes the amount of local-zodi-induced noise that is present after the nulling independent from the length of the chosen interferometric baseline.

Therefore, toward longer wavelengths the instrument sensitivity is independent from the observed target.[14] At short wavelengths, the noise is dominated by the host star. As the flux ratio between the exoplanet and its host star becomes more favorable toward later stellar types, the sensitivity of the observations increases for such star types. Coupled with more prominent spectra features, this results in the demonstrated higher significance detection in the shorter wavelength bands for the M-star targets compared to the G- and K-star targets.

4.2. Golden Targets and Dynamic Atmospheric Signatures

One of the most interesting outcomes of this analysis is the expected quality of data obtainable for the closest target planets. For example for the Proxima Centauri case at the original distance (see Figure 8) or similar cases within <3 pc distance from the Sun, "spectral temporal resolution" of a few days is possible, meaning that changes caused by fluxes of the same magnitude assumed in our models could be detected on timescales of days or weeks. This could be used to characterize exoplanetary variability and dynamic processes in the atmosphere.

4.3. Consequences for Science and Technology Requirements

Figure 9 shows the dependence of the observation time needed to constrain N$_2$O for the 10 Tmol yr^{-1} Earth-twin case with various design parameters of the LIFE mission. The bottom plot of Figure 9 shows a relatively weak dependence on the shorter wavelength cut off but a very strong dependence on the longer wavelength which is explained by the location of the N$_2$O features in the MIR for the G star case.[15] The Figure 9 center panel shows how for the 2 m mirror size at 5% throughput (or an equivalent size/throughput combination) it would take about 15 days to reach the 10 sigma band-integrated threshold while it would only take about 5 days in the 3.5 m configuration. For a descoped 1 m setup we would not reach that in a reasonable time (>100 days). Figure 9 top panel shows almost no dependence on spectral resolution, due to the relatively wide bands of N$_2$O.

4.4. Synergies and Comparison With Other Observational Platforms

Schwieterman et al. (2022) and Leung et al. (2022) showed that some of the scenarios discussed here may be observable with JWST in transiting systems such as TRAPPIST-1. However, these observations would need to add the signal from 10–100 s of individual transits and will therefore only be feasible for very few, selected, transiting planets around very late-type stars. On the other hand, it was shown that the long baselines of LIFE, which result in extremely high spatial resolution will be particularly well suited for systems around late-type stars very close to habitable zones, that are also inaccessible to direct imaging techniques at shorter wavelengths (Dannert et al. 2022; Carrión-González et al. 2023, see also Figure 1). Furthermore, N$_2$O shows orders of magnitude

---

[14] The local-zodi noise does strongly depend on the position of the target in relation to the ecliptic plane Dannert et al. (2022), which is kept equal ($lat_s = 0.78$) for all cases simulated in the "characterization phase" in this study.
[15] It is important to note that in full retrievals, the contextual information provided by other wavelength bands is very important to constrain the abundances. This fact is not included in this analysis and should hence be taken with a grain of salt.
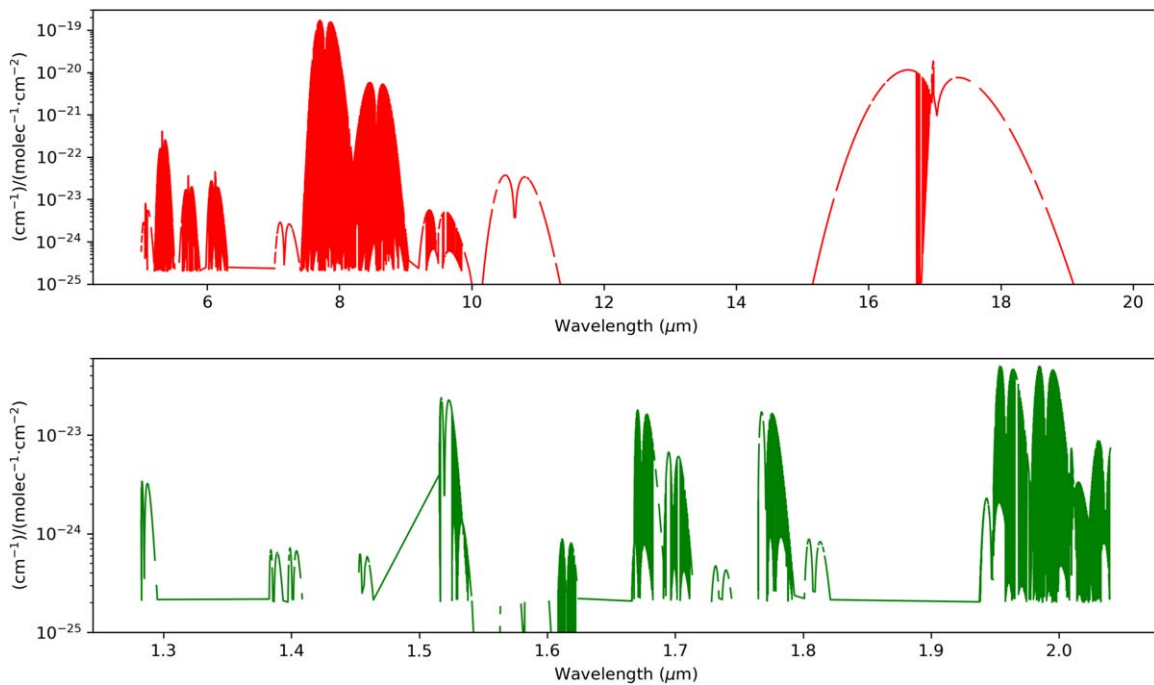
Figure 10. HITRAN line intensities for N_2O showing orders of magnitude stronger features in the MIR versus the NIR. This comparison is not possible for CH_3Br/CH_3Cl, because their absolute cross sections have not been systematically measured in the 0.2–2 μm region relevant to reflected light observations of terrestrial planets (e.g., HWO).

difference in the line intensities between the strongest MIR regions and the strongest NIR regions (see Figure 10). The ability to characterize terrestrial temperate exoplanets around late-type stars and the access to molecules that only show strong features in the MIR are two of the main synergies of LIFE with HWO, which will mostly focus on FGK systems and observe in the UV to NIR range.

If there are late-type star exoplanetary systems in the solar neighborhood with planets that exhibit global biospheres producing N_2O and CH_3X signals, LIFE will be the best-suited future mission to systematically search for and eventually detect them.

4.5. Summary of Results

1. Our first-order analysis of the detectability of exoplanetary spectra with the modeled fluxes of potentially biogenic gases shows that most of the discussed cases are indeed observable with a space telescope like LIFE with observation times between 10 and 100 days for habitable planetary systems within 5 pc.

2. We compare some of these results to selected retrievals, confirm the detectability, and generally show consistency with the direct comparison of forward models in the detectability metric used here.

3. Using simulations of potential yields of the LIFE mission we can show that dozens of terrestrial temperate exoplanets can be tested for these molecules in the way discussed here. In terms of distance, the cases at 5 pc are typical for M-star hosts and likely the best cases for FGK hosts.

4. For some "golden targets" (e.g., a very nearby system like Proxima Centauri) LIFE could detect levels of the discussed species on very short timescales, delivering

high "spectral-temporal" resolution of days to week to observe 10 s of Tmol yr^{-1} fluxes, potentially opening up future avenues for variability studies.

5. Comparison of the LIFE baseline with other potential setups of the space telescope confirms observability also for different instrumental configurations and informs the mission design about tradeoffs driven by the detectability of these features.

Appendix A
Retrieval Details

In this appendix section, we show the corner plots with all posteriors, the derived pressure–temperature profiles, and the fitted spectra (Figures A1–A3) as well as the derived parameters (Tables A1–A3) for the three cases discussed in Section 3.4.
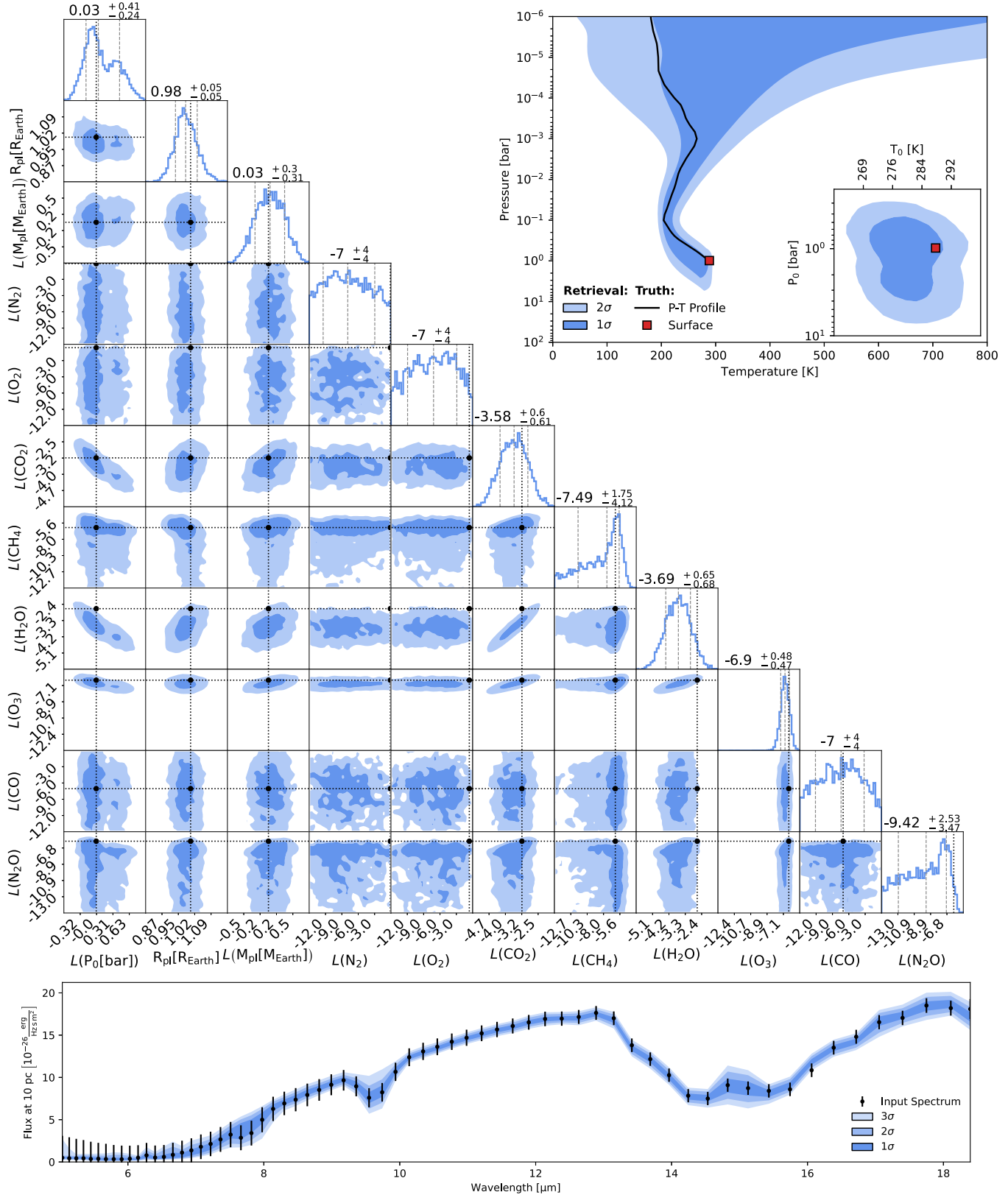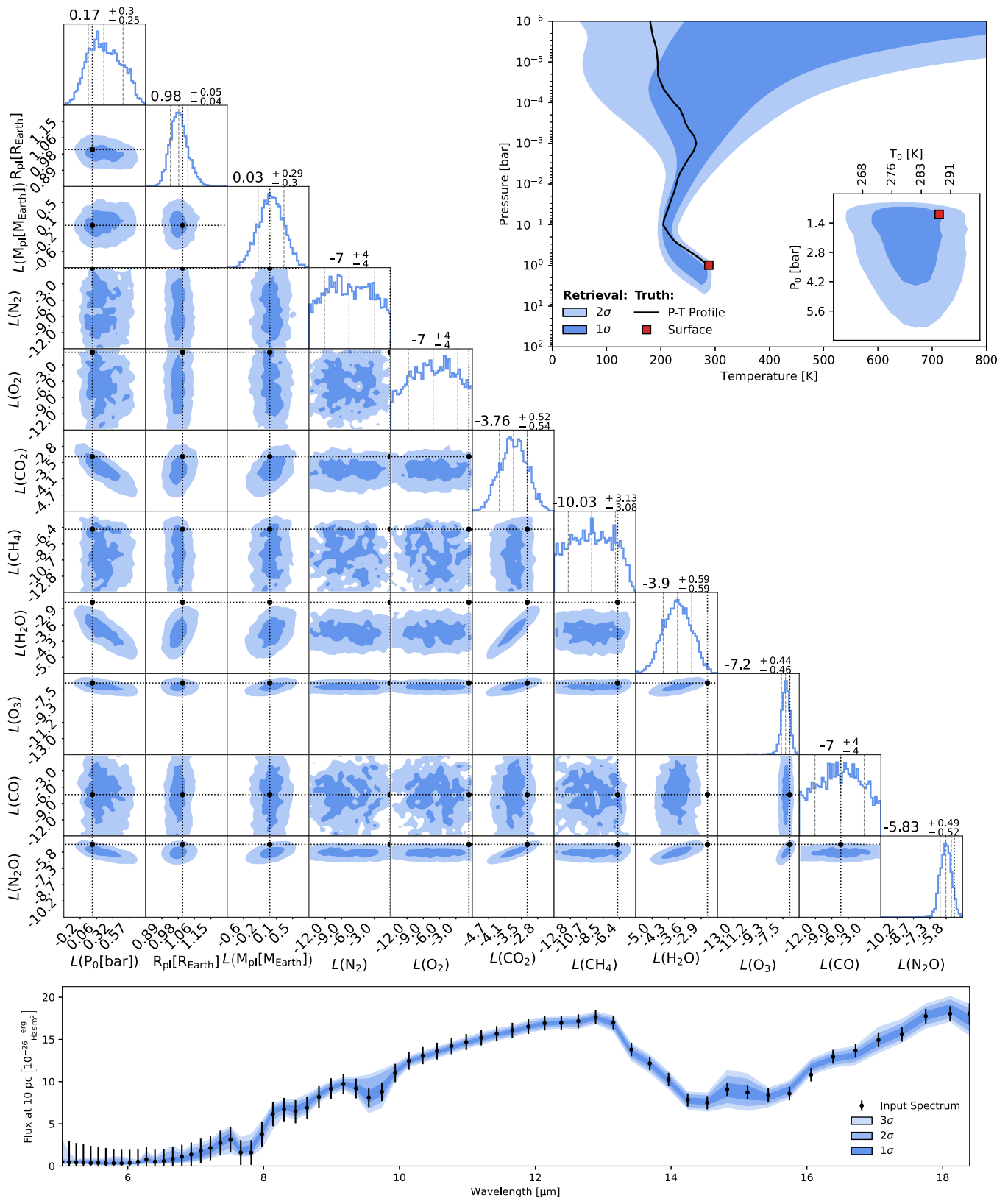

Figure A1. Retrieval results for 1 Tmol yr^{-1} N$_2$O case.
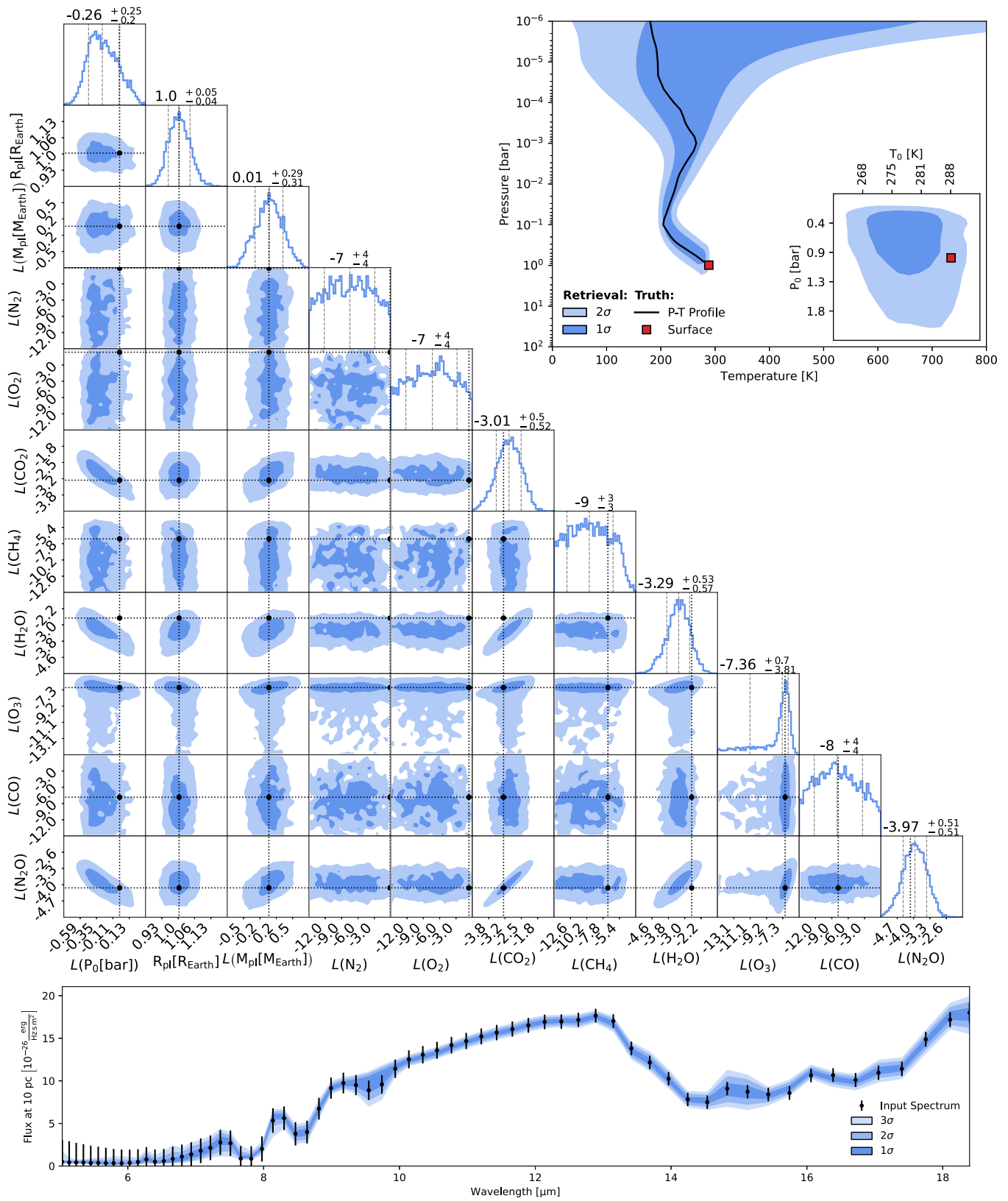
Figure A2. Retrieval results for 10 Tmol yr^{-1} N$_2$O case.

Figure A3. Retrieval results for 100 Tmol yr^{-1}N$_2$O case.

Table A1
1 Tmol yr^{-1} Retrieval Results

Value	Retrieved result
$L(P_0[\text{bar}])$	$0.03\ ^{+0.41}_{-0.24}$
$R_{pl}[R_{\text{Earth}}]$	$0.98\ ^{+0.05}_{-0.05}$
$L(M_{pl}[M_{\text{Earth}}])$	$0.03\ ^{+0.30}_{-0.31}$
$L(N_2)$	$\cdots$
$L(O_2)$	$\cdots$
$L(CO_2)$	$-3.58\ ^{+0.60}_{-0.61}$
$L(CH_4)$	$-7.49\ ^{+1.75}_{-4.12}$
$L(H_2O)$	$-3.69\ ^{+0.65}_{-0.68}$
$L(O_3)$	$-6.90\ ^{+0.48}_{-0.47}$
$L(CO)$	$\cdots$
$L(N_2O)$	$-9.42\ ^{+2.53}_{-3.47}$

Note. Here, $L(\,\cdot\,)$ Stands for $\log_{10}(\cdot)$.

Table A2
10 Tmol yr^{-1} Retrieval Results

Value	Retrieved result
$L(P_0[\text{bar}])$	$0.17\ ^{+0.30}_{-0.25}$
$R_{pl}[R_{\text{Earth}}]$	$0.98\ ^{+0.05}_{-0.04}$
$L(M_{pl}[M_{\text{Earth}}])$	$0.03\ ^{+0.29}_{-0.30}$
$L(N_2)$	$\cdots$
$L(O_2)$	$\cdots$
$L(CO_2)$	$-3.76\ ^{+0.52}_{-0.54}$
$L(CH_4)$	$-10\ ^{+3}_{-3}$
$L(H_2O)$	$-3.90\ ^{+0.59}_{-0.59}$
$L(O_3)$	$-7.20\ ^{+0.44}_{-0.46}$
$L(CO)$	$\cdots$
$L(N_2O)$	$-5.83\ ^{+0.49}_{-0.52}$

Note. Here, $L(\,\cdot\,)$ Stands for $\log_{10}(\cdot)$.

Table A3
100 Tmol yr^{-1} Retrieval Results

Value	Retrieved result
$L(P_0[\text{bar}])$	$-0.26\ ^{+0.25}_{-0.20}$
$R_{pl}[R_{\text{Earth}}]$	$1.00\ ^{+0.05}_{-0.04}$
$L(M_{pl}[M_{\text{Earth}}])$	$0.01\ ^{+0.31}_{-0.29}$
$L(N_2)$	$\cdots$
$L(O_2)$	$\cdots$
$L(CO_2)$	$-3.01\ ^{+0.50}_{-0.52}$
$L(CH_4)$	$-9\ ^{+3}_{-3}$
$L(H_2O)$	$-3.29\ ^{+0.53}_{-0.57}$
$L(O_3)$	$-7.36\ ^{+0.70}_{-3.81}$
$L(CO)$	$\cdots$
$L(N_2O)$	$-3.97\ ^{+0.51}_{-0.51}$

Note. Here, $L(\,\cdot\,)$ Stands for $\log_{10}(\cdot)$.

Appendix B
Modeled Observations for Different Observation Times

In the following two appendix sections, we show the simulated observations for 10 and 100 days of observation in addition to the 50 day observations already shown in the main text.

B.1. Supplementary Results N2O

In this section we provide the figures for 10 and 100 day observations of N_2O (Figures B1 and B2).
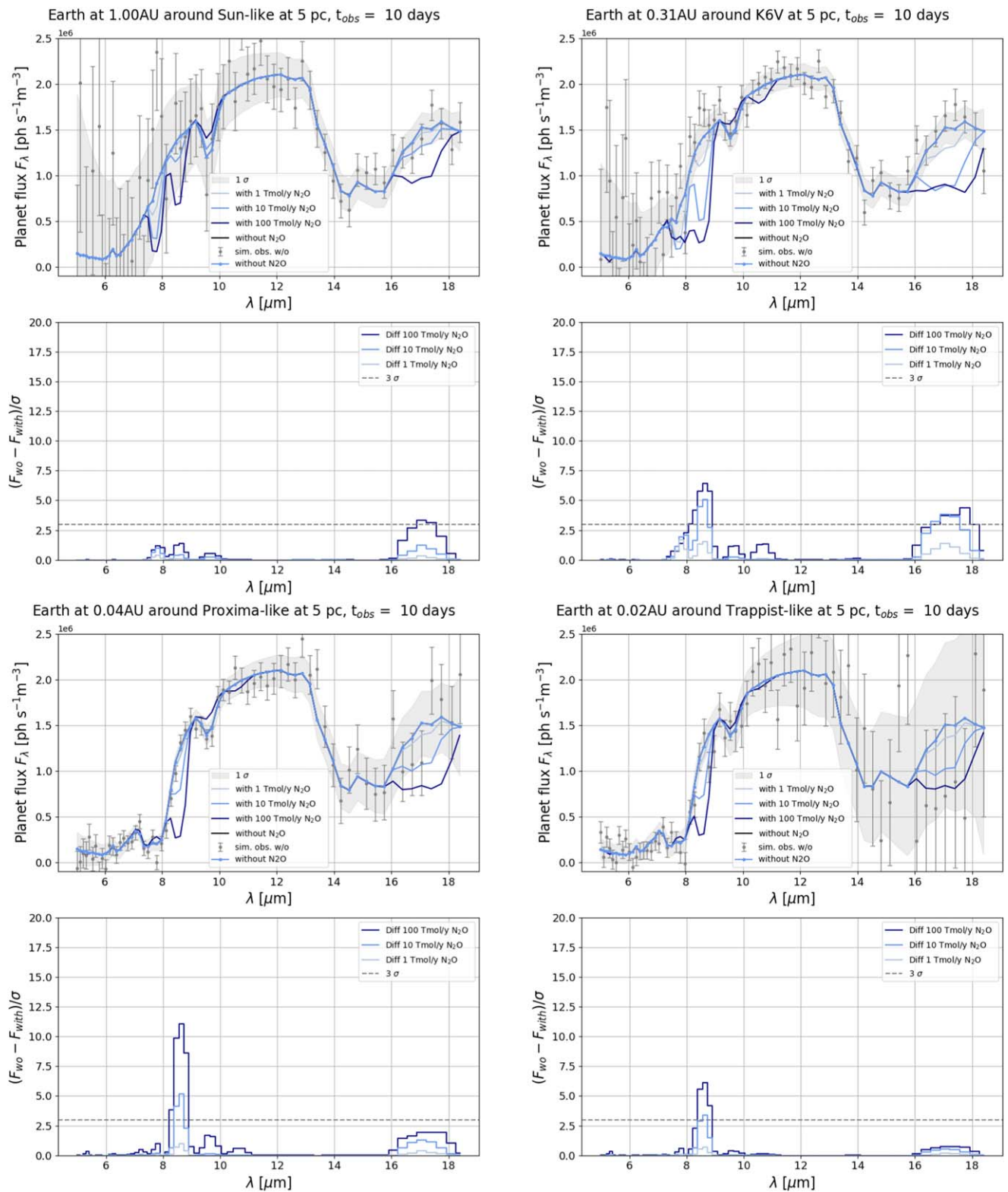
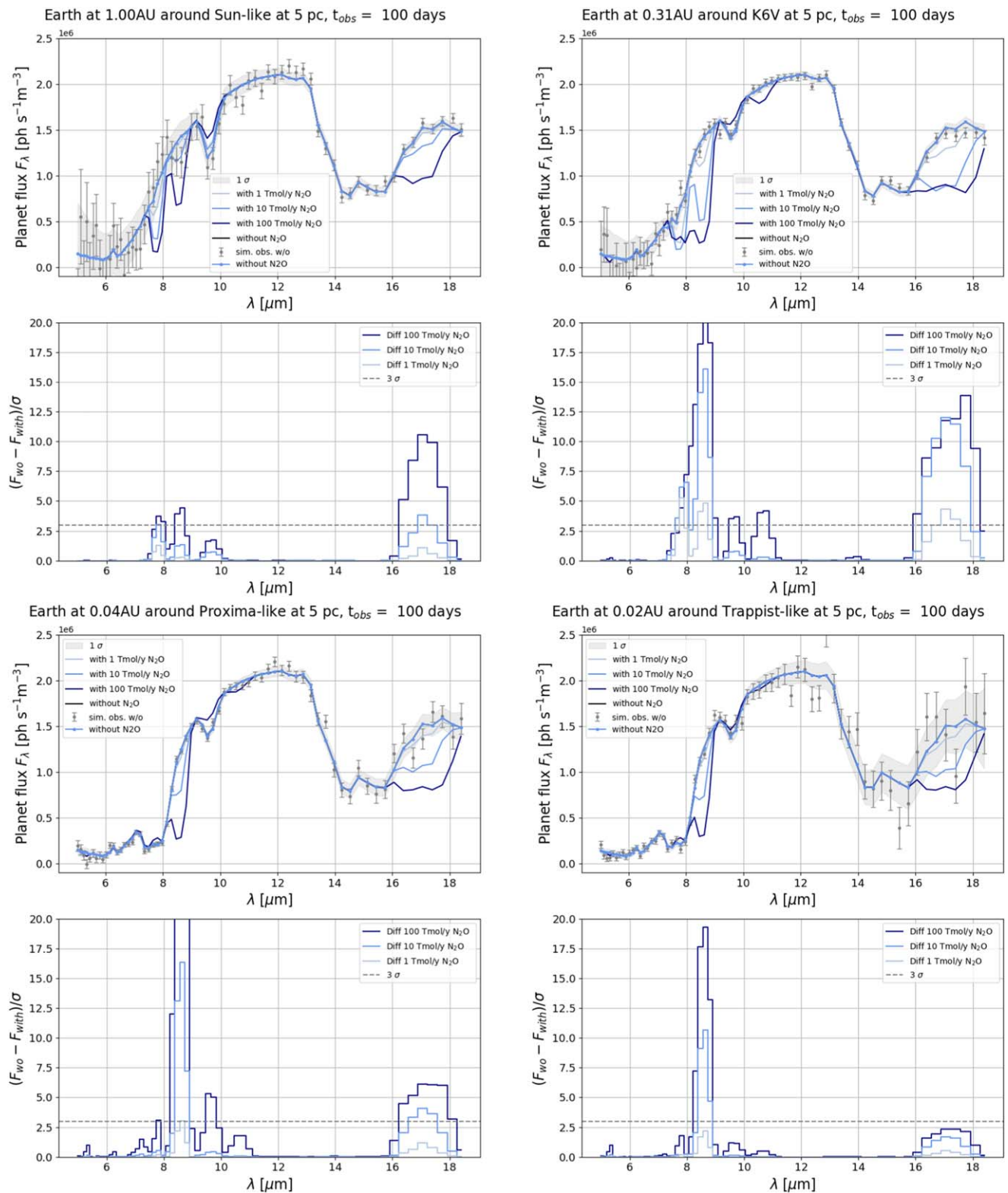**Figure B1.** Same as Figure 2 for 10 days of observation time.

Figure B2. Same as Figure 2 for 100 days of observation time.

B.2. Supplementary Results CH3x

In this section we provide the figures for 10 and 100 day observations of CH$_{3X}$ for a Proxima-Centauri type host (Figures B3 and B4), AD Leonis-type host (Figures B5 and B6), K6V-type host (Figures B7 and B8), and a TRAPPIST-1 type host (Figures B9 and B10).
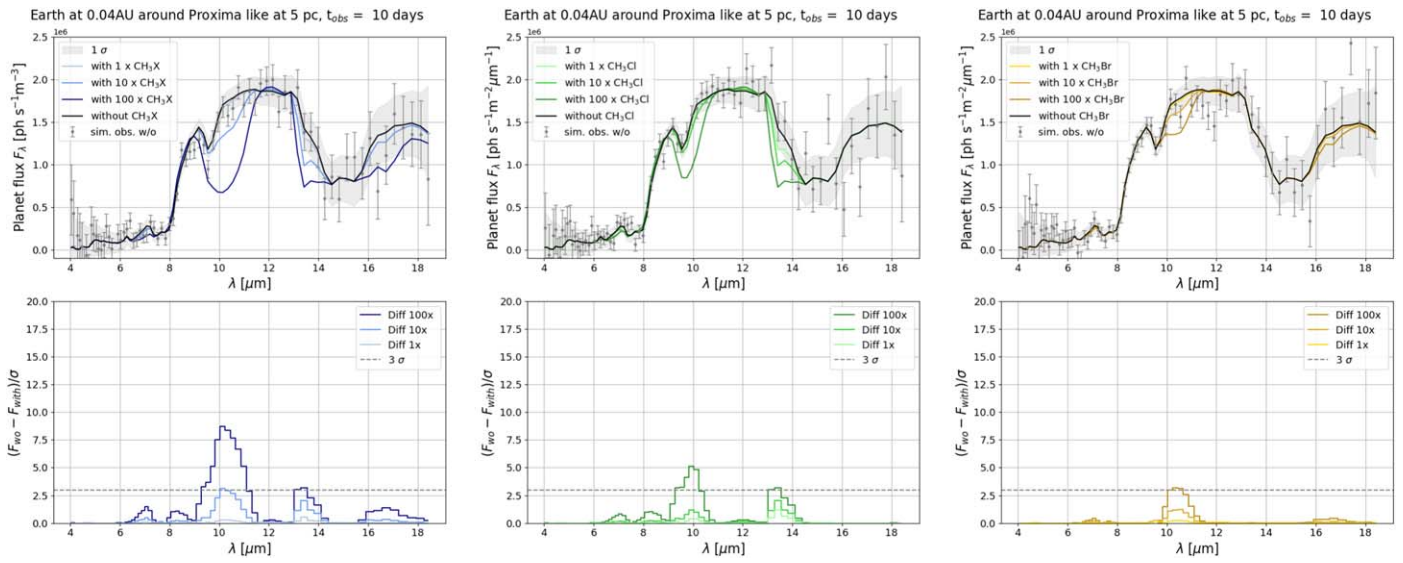
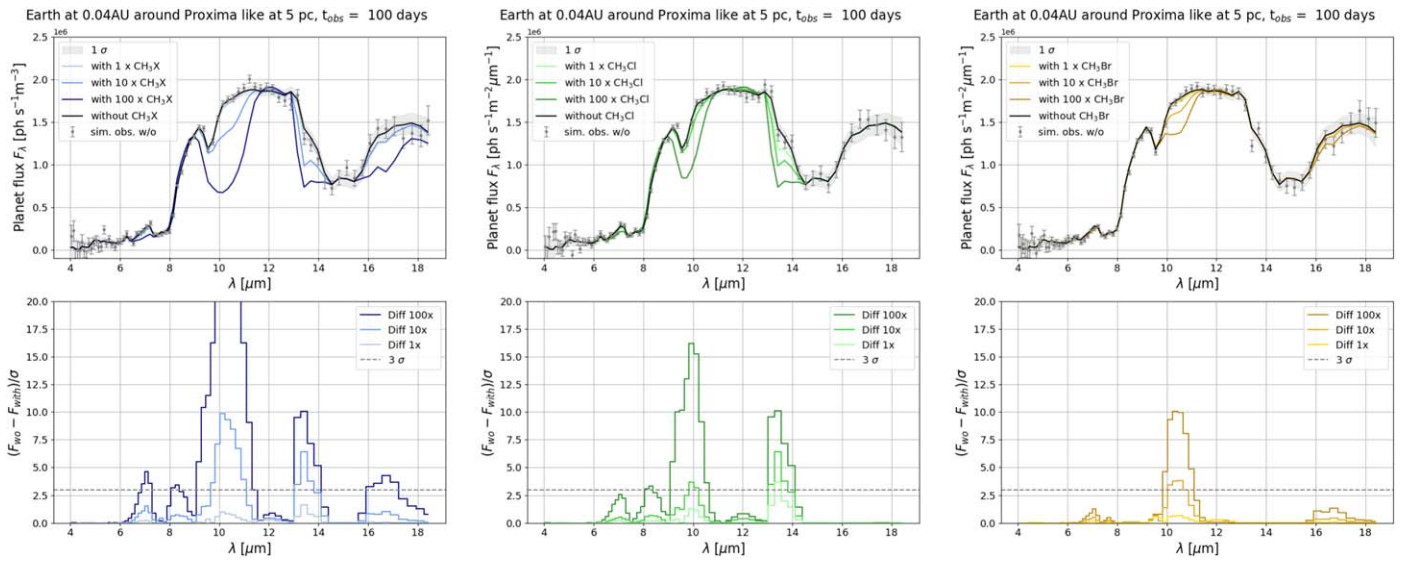**Figure B3.** Results for Proxima-type star in 10 days.

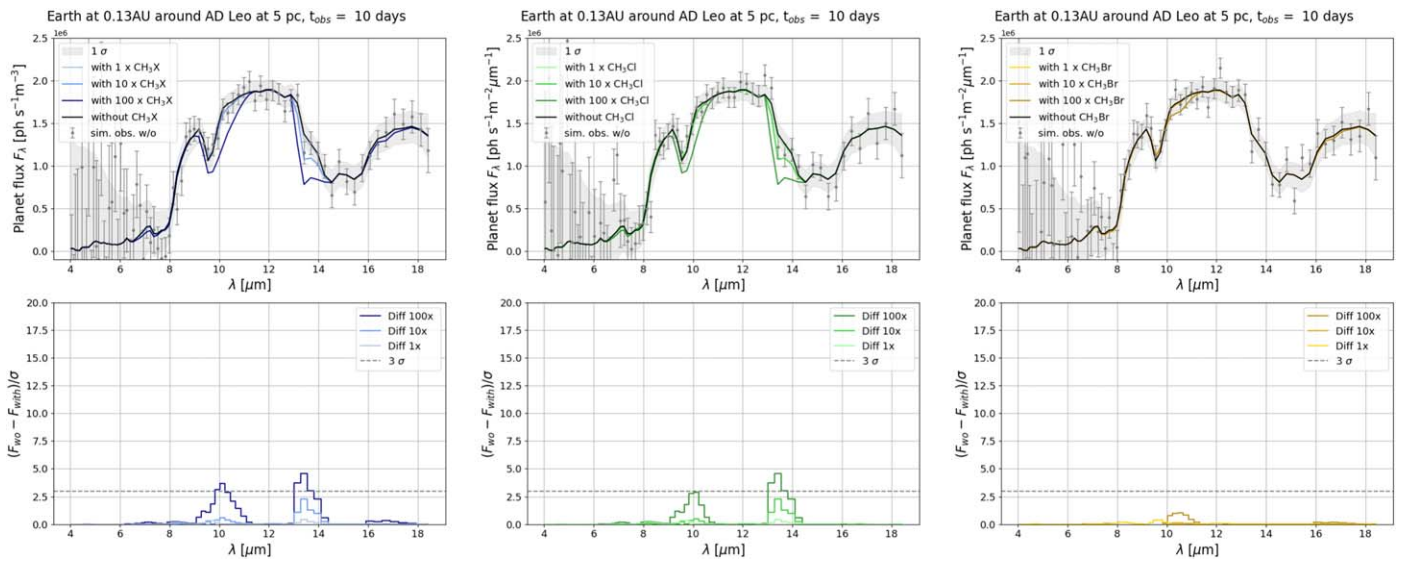**Figure B4.** Results for Proxima-type star in 100 days.

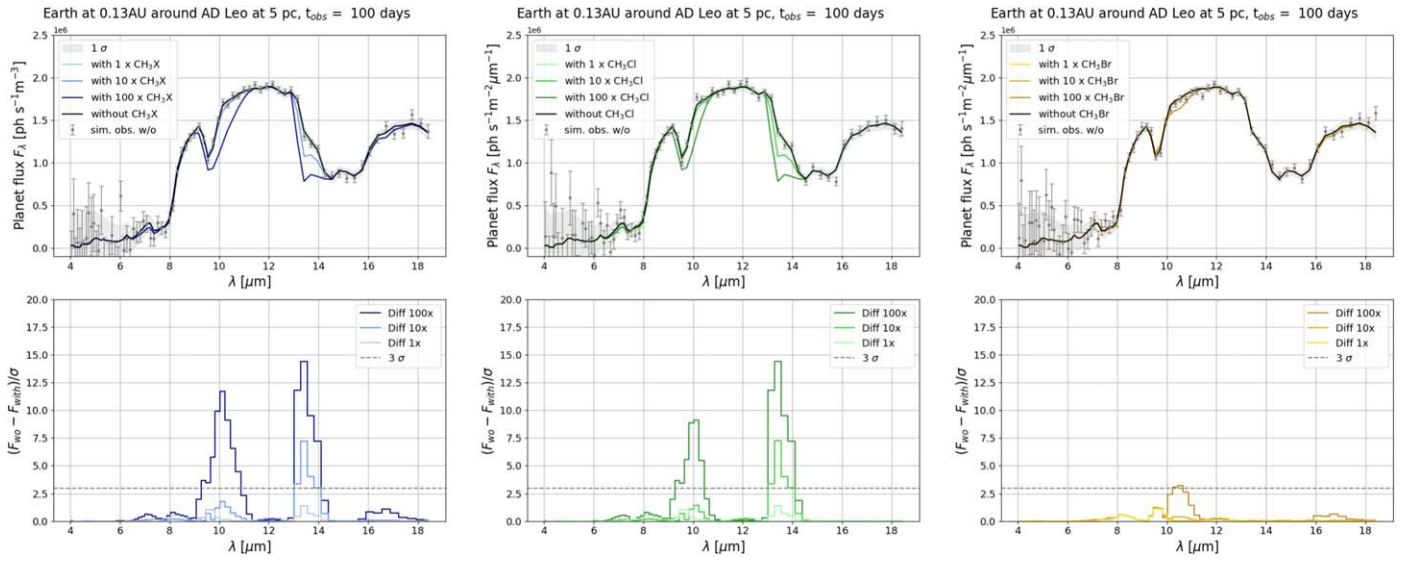**Figure B5.** Results for AD Leonis–type star in 10 days.

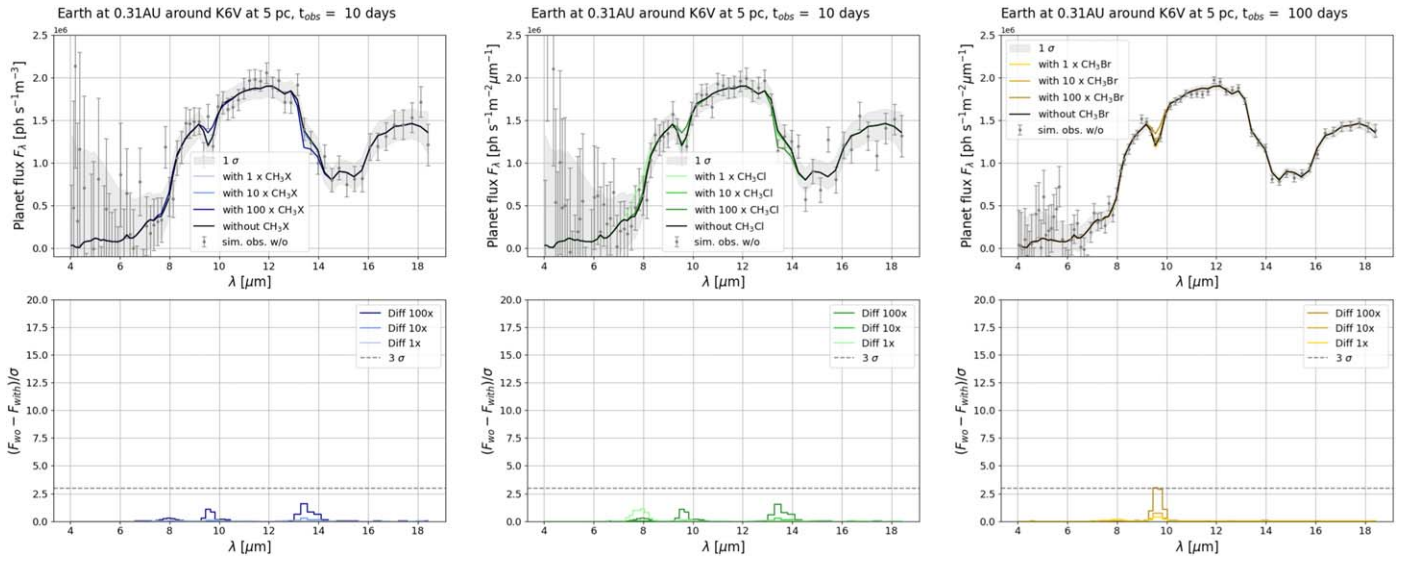**Figure B6.** Results for AD Leonis–type star in 100 days.

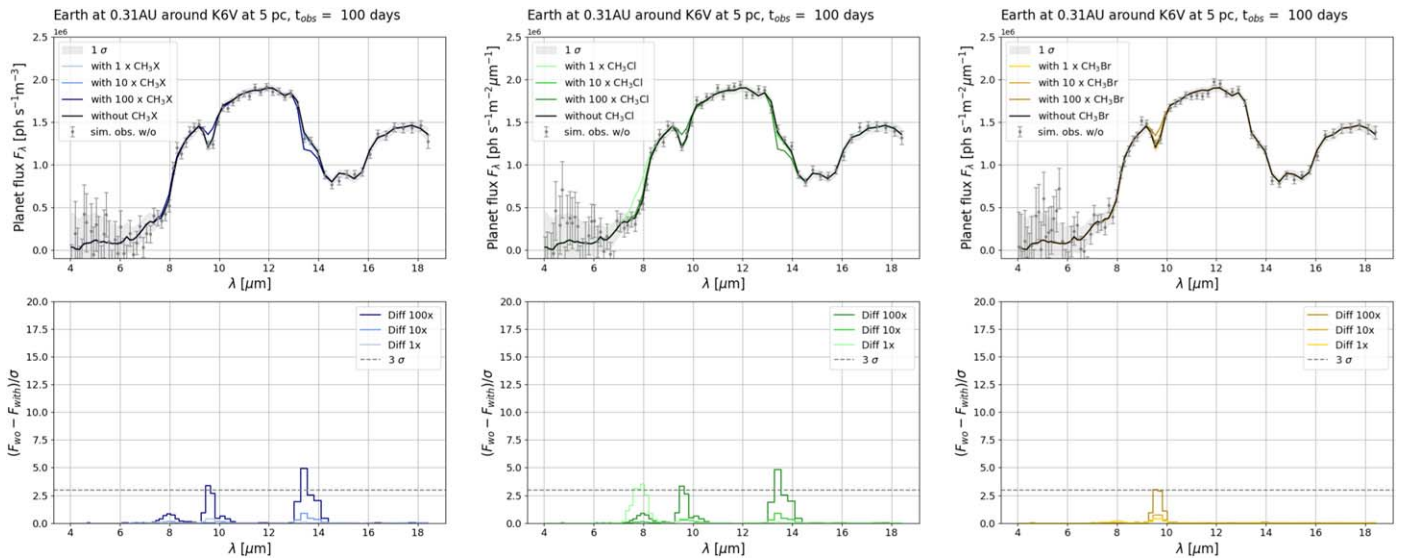**Figure B7.** Results for K6V-type star in 10 days.

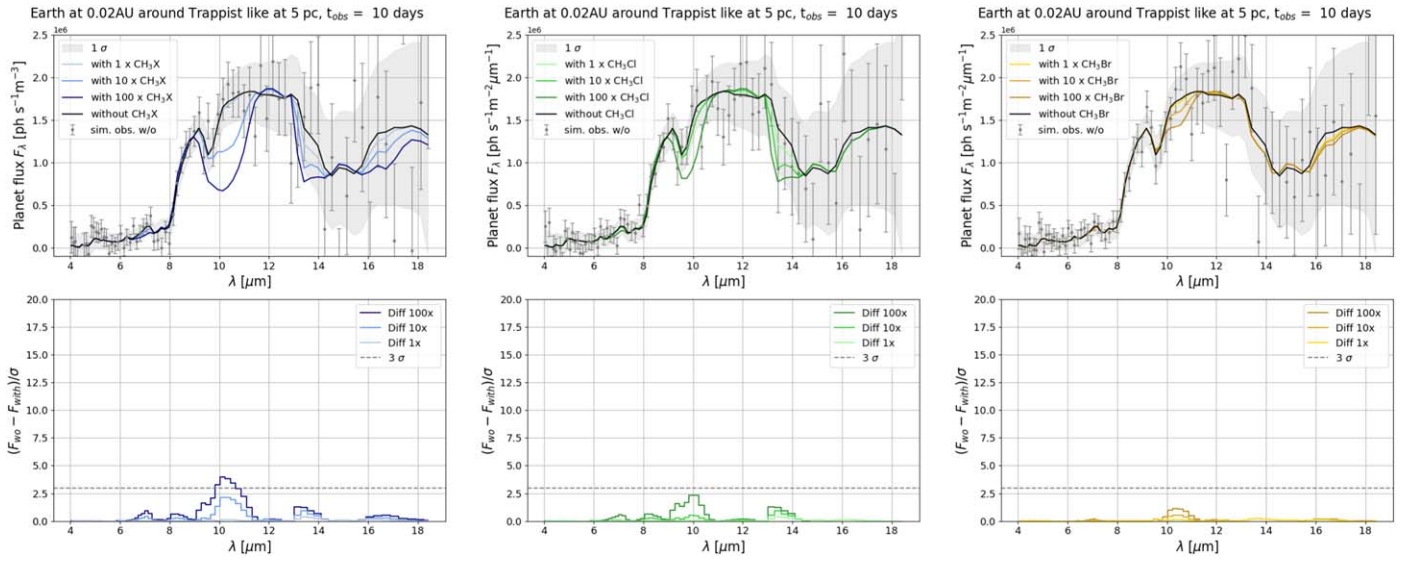**Figure B8.** Results for K6V-type star in 100 days.

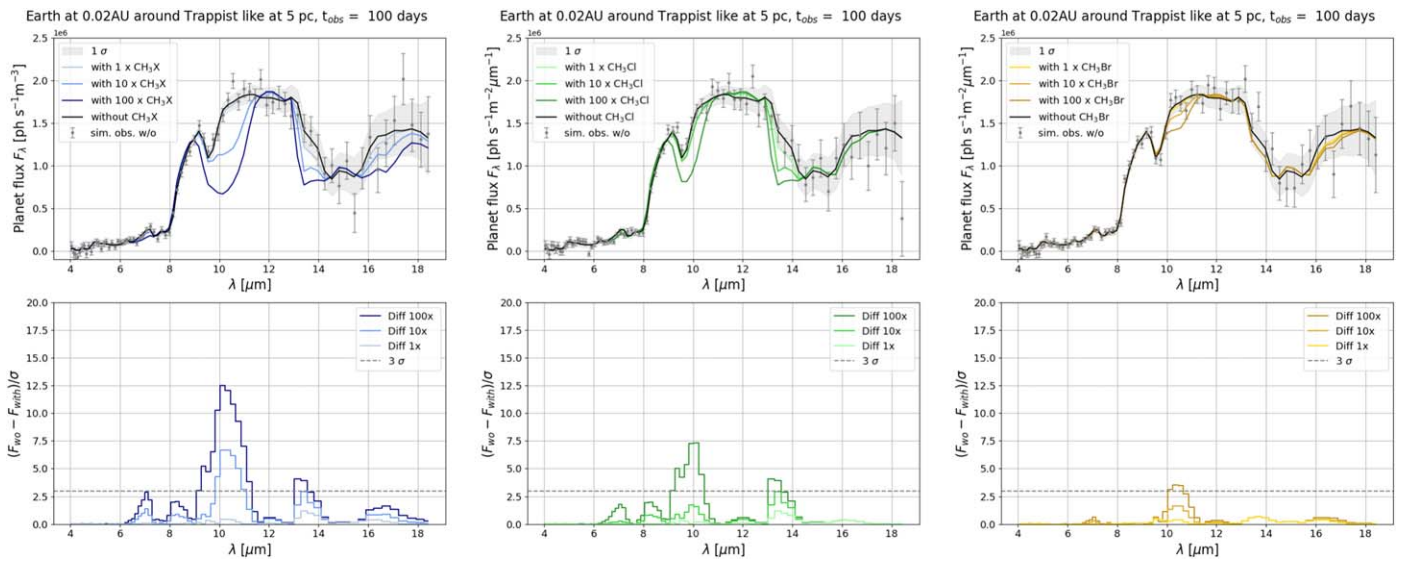**Figure B9.** Results for TRAPPIST-1 type star in 10 days.

Figure B10. Results for TRAPPIST-1 type star in 100 days.

Appendix C
N_2O and CH_3X Flux-abundance Details

The predicted abundance of a trace gas, while highly dependent on its production flux, can also vary as a function of the background atmosphere and other assumptions embedded in the photochemical model used to calculate it including fundamental inputs such as stellar spectra, reaction rates, and

molecular cross sections (e.g., Ranjan et al. 2020). To facilitate future reproduction of our results, in Tables C1 and C2 we provide a cross-referencing of the N_2O and CH_3X fluxes and their respective predicted ground-level mixing ratios used in this study. As stated above, these calculations are sourced from Schwieterman et al. (2022) for N_2O and Leung et al. (2022) for CH_3Cl, CH_3Br, and CH_3X.

Table C1
Flux vs. Ground-level Abundance for N_2O

Scenario	Earth-like Flux	1 Tmol yr^{-1}	10 Tmol yr^{-1}	100 Tmol yr^{-1}
Sun	3.39×10^{-7}	7.34×10^{-7}	5.44×10^{-6}	4.54×10^{-5}
K6V	2.96×10^{-6}	7.20×10^{-6}	9.14×10^{-5}	1.63×10^{-3}
Proxima Centauri	1.14×10^{-6}	2.75×10^{-6}	2.82×10^{-5}	6.54×10^{-4}
TRAPPIST-1	1.27×10^{-6}	3.08×10^{-6}	3.09×10^{-5}	3.26×10^{-4}

Table C2
Flux vs. Ground-level Abundance for CH_3Cl, CH_3Br, and C_3X

Scenario	Earth-like Flux	10× Earth-like Flux	100× Earth-like Flux	1000× Earth-like Flux
K6V-CH_3Cl	4.82×10^{-9}	4.82×10^{-8}	3.64×10^{-7}	2.09×10^{-6}
K6V-CH_3Br	1.28×10^{-10}	1.23×10^{-9}	1.05×10^{-8}	1.34×10^{-7}
K6V-CH_3X	4.94×10^{-9}	4.94×10^{-8}	3.73×10^{-7}	2.11×10^{-6}
AD Leo-CH_3Cl	5.92×10^{-8}	5.02×10^{-7}	3.43×10^{-6}	3.69×10^{-5}
AD Leo-CH_3Br	3.47×10^{-9}	3.42×10^{-8}	4.61×10^{-7}	1.49×10^{-6}
AD Leo-CH_3X	6.27×10^{-8}	5.39×10^{-7}	3.57×10^{-6}	4.77×10^{-5}
Proxima Centauri-CH_3Cl	5.38×10^{-7}	1.64×10^{-6}	1.34×10^{-5}	1.40×10^{-4}
Proxima Centauri-CH_3Br	1.15×10^{-7}	7.77×10^{-7}	2.86×10^{-6}	9.39×10^{-6}
Proxima Centauri-CH_3X	2.87×10^{-7}	3.80×10^{-6}	3.21×10^{-5}	3.94×10^{-4}
TRAPPIST-1-CH_3Cl	1.26×10^{-7}	1.18×10^{-6}	9.65×10^{-6}	7.45×10^{-5}
TRAPPIST-1-CH_3Br	9.81×10^{-8}	4.47×10^{-7}	1.24×10^{-6}	4.60×10^{-6}
TRAPPIST-1-CH_3X	2.24×10^{-7}	4.30×10^{-6}	2.14×10^{-5}	6.16×10^{-4}

ORCID iDs

Daniel Angerhausen https://orcid.org/0000-0001-6138-8633
Daria Pidhorodetska https://orcid.org/0000-0001-9771-7953
Michaela Leung https://orcid.org/0000-0003-1906-5093
Janina Hansen https://orcid.org/0009-0003-1247-8378
Eleonora Alei https://orcid.org/0000-0002-0006-1175
Felix Dannert https://orcid.org/0000-0002-5476-2663
Jens Kammerer https://orcid.org/0000-0003-2769-0438
Sascha P. Quanz https://orcid.org/0000-0003-3829-7412
Edward W. Schwieterman https://orcid.org/0000-0002-2949-2163

References

Alei, E., Konrad, B. S., Mollière, P., et al. 2022a, Proc. SPIE, 12180, 121803L
Alei, E., Konrad, B. S., Angerhausen, D., et al. 2022b, A&A, 665, A106
Angerhausen, D., Ottiger, M., Dannert, F., et al. 2023, AsBio, 23, 183
Arney, G., Domagal-Goldman, S. D., Meadows, V. S., et al. 2016, AsBio, 16, 873
Arney, G., Meadows, V., Crisp, D., et al. 2014, JGRE, 119, 1860
Arney, G. N., Meadows, V. S., Domagal-Goldman, S. D., et al. 2017, ApJ, 836, 49
Ben-Ami, S., López-Morales, M., & Szentgyorgyi, A. 2018, Proc. SPIE, 10702, 107026N
Bixel, A., & Apai, D. 2021, AJ, 161, 228
Bryson, S., Kunimoto, M., Kopparapu, R. K., et al. 2021, AJ, 161, 36
Buchner, J., Georgakakis, A., Nandra, K., et al. 2014, A&A, 564, A125
Buick, R. 2007, Gbio, 5, 97
Chen, H., Wolf, E. T., Kopparapu, R., Domagal-Goldman, S., & Horton, D. E. 2018, ApJL, 868, L6
Dannert, F. A., Ottiger, M., Quanz, S. P., et al. 2022, A&A, 664, A22
Des Marais, D. J., Harwit, M. O., Jucks, K. W., et al. 2002, AsBio, 2, 153
Domagal-Goldman, S. D., Meadows, V. S., Claire, M. W., & Kasting, J. F. 2011, AsBio, 11, 419
Dressing, C. D., & Charbonneau, D. 2015, ApJ, 807, 45
Ertel, S., Defrère, D., Hinz, P., et al. 2018, AJ, 155, 194
Ertel, S., Defrère, D., Hinz, P., et al. 2020, AJ, 159, 177
France, K., Loyd, R. O. P., Youngblood, A., et al. 2016, ApJ, 820, 89
Fuge, R. 1988, EnvGH, 10, 51
Fujii, Y., Angerhausen, D., Deitrick, R., et al. 2018, AsBio, 18, 739
Gaia Collaboration, Brown, A. G. A., Vallenari, A, et al. 2018, A&A, 616, A1
Gaudi, B. S., Seager, S., Mennesson, B., et al. 2020, arXiv:2001.06683
Gordon, I. E., Rothman, L. S., Hargreaves, R. J., et al. 2022, JQSRT, 277, 107949
Greene, T. P., Line, M. R., Montero, C., et al. 2016, ApJ, 817, 17
Hansen, J. T., Ireland, M. J. & LIFE Collaboration 2022, A&A, 664, A52
Hansen, J. T., Ireland, M. J., Laugier, R. & LIFE Collaboration 2023, A&A, 670, A57
Janson, M., Patel, J., Ringqvist, S. C., et al. 2023, A&A, 671, A114
Jia, G., Fu, Y., & He, C. 2013, Trends Genet., 29, 108
Carrión-González, Ó., Kammerer, J., Angerhausen, D., et al. 2023, A&A, 678, A96
Kammerer, J., & Quanz, S. P. 2018, A&A, 609, A4
Kammerer, J., Quanz, S. P., Dannert, F. & LIFE Collaboration 2022, A&A, 668, A52
Kasdin, N. J., Bailey, V. P., Mennesson, B., et al. 2020, Proc. SPIE, 11443, 114431U
Kasting, J. F., Liu, S. C., & Donahue, T. M. 1979, JGR, 84, 3097
Konrad, B. S., Alei, E., Quanz, S. P., et al. 2022, A&A, 664, A23
Konrad, B. S., Alei, E., Quanz, S. P., et al. 2023, A&A, 673, A94
Kopparapu, R. K., Hébrard, E., Belikov, R., et al. 2018, ApJ, 856, 122
Kopparapu, R. K., Ramirez, R. M., SchottelKotte, J., et al. 2014, ApJL, 787, L29
Krissansen-Totton, J., Olson, S., & Catling, D. C. 2018, SciA, 4, eaao5747
Leung, M., Schwieterman, E. W., Parenteau, M. N., & Fauchez, T. J. 2022, ApJ, 938, 6
Lincowski, A. P., Meadows, V. S., Crisp, D., et al. 2018, ApJ, 867, 76
Lovis, C., Snellen, I., Mouillet, D., et al. 2017, A&A, 599, A16
Loyd, R. O. P., France, K., Youngblood, A., et al. 2016, ApJ, 824, 102
Loyd, R. O. P., France, K., Youngblood, A., et al. 2018, ApJ, 867, 71
Lustig-Yaeger, J., Meadows, V. S., & Lincowski, A. P. 2019, AJ, 158, 27
Matsuo, T., Dannert, F., Laugier, R., et al. 2023, A&A, 678, A97
Meadows, V. S., Arney, G. N., Schwieterman, E. W., et al. 2018a, AsBio, 18, 133
Meadows, V. S., & Crisp, D. 1996, JGR, 101, 4595
Meadows, V. S., Reinhard, C. T., Arney, G. N., et al. 2018b, AsBio, 18, 630
Mollière, P., Wardenier, J. P., van Boekel, R., et al. 2019, A&A, 627, A67
Morley, C. V., Kreidberg, L., Rustamkulov, Z., Robinson, T., & Fortney, J. J. 2017, ApJ, 850, 121
Murray, N. J., Worthington, T. A., Bunting, P., et al. 2022, Sci, 376, 744

National Academies of Sciences E. & Medicine 2021, Pathways to Discovery in Astronomy and Astrophysics for the 2020s (Washington, DC: The National Academies Press)
Pavlov, A. A., Brown, L. L., & Kasting, J. F. 2001, JGR, 106, 23267
Peacock, S., Barman, T., Shkolnik, E. L., Hauschildt, P. H., & Baron, E. 2019, ApJ, 871, 235
Peacock, S., Barman, T., Shkolnik, E. L., et al. 2020, ApJ, 895, 5
Prather, M. J., Hsu, J., DeLuca, N. M., et al. 2015, JGRD, 120, 5693
Prosser, J. I., & Nicol, G. W. 2012, Trends in Microbiol., 20, 523
Quanz, S. P., Absil, O., Angerhausen, D., et al. 2019, arXiv:1908.01316
Quanz, S. P., Kammerer, J., Defrère, D., et al. 2018, Proc. SPIE, 10701, 107011I
Quanz, S. P., Ottiger, M., Fontanet, E., et al. 2022, A&A, 664, A21
Ranjan, S., Schwieterman, E. W., Harman, C., et al. 2020, ApJ, 896, 148
Robinson, T. D., Meadows, V. S., Crisp, D., et al. 2011, AsBio, 11, 393
Schwieterman, E. W., Kiang, N. Y., Parenteau, M. N., et al. 2018, AsBio, 18, 663
Schwieterman, E. W., Olson, S. L., Pidhorodetska, D., et al. 2022, ApJ, 937, 109
Seager, S., Bains, W., & Petkowski, J. J. 2016, AsBio, 16, 465
Segura, A. A., Kasting, J. F., Meadows, V., et al. 2005, AsBio, 5, 706
Shkolnik, E. L., & Barman, T. S. 2014, AJ, 148, 64
Snellen, I. A. G., de Kok, R. J., le Poole, R., Brogi, M., & Birkby, J. 2013, ApJ, 764, 182
Sousa-Silva, C., Seager, S., Ranjan, S., et al. 2020, AsBio, 20, 235
Stark, C. C., Belikov, R., Bolcar, M. R., et al. 2019, JATIS, 5, 024009
Tait, V. K., & Moore, R. M. 1995, LimOc, 40, 189
The LUVOIR Team 2019, arXiv:1912.06219
Thompson, S. E., Coughlin, J. L., Hoffman, K., et al. 2018, ApJS, 235, 38
Thuillier, G., Floyd, L., Woods, T. N., et al. 2004, AdSpR, 34, 256
Tian, H., Xu, R., Canadell, J. G., et al. 2020, Natur, 586, 248
Tinetti, G., Drossart, P., Eccleston, P., et al. 2018, ExA, 46, 135
Villanueva, G. L., Liuzzi, G., Faggi, S., et al. 2022, Fundamentals of the Planetary Spectrum Generator (Washington, DC: NASA)
Villanueva, G. L., Smith, M. D., Protopapa, S., Faggi, S., & Mandell, A. M. 2018, JQSRT, 217, 86
Yang, L., Zhang, S., Yin, L., & Zhang, B. 2022, Ecol. Indic., 142, 109307
Zahnle, K., Claire, M., & Catling, D. 2006, Gbio, 4, 271
Zhu, Z., Piao, S., Myneni, R. B., et al. 2016, NatCC, 6, 791